

# Computer-Aided Light Sheet Flow Visualization Using Photogrammetry

---

*Kathryn Stacy, Kurt Severance, and Brooks A. Childers*  
*Langley Research Center • Hampton, Virginia*

The use of trademarks or names of manufacturers in this report is for accurate reporting and does not constitute an official endorsement, either expressed or implied, of such products or manufacturers by the National Aeronautics and Space Administration.

## Abstract

*A computer-aided flow visualization process has been developed to analyze video images acquired from rotating and translating light sheet visualization systems. The computer process integrates a mathematical model for image reconstruction, advanced computer graphics concepts, and digital image processing to provide a quantitative and a visual analysis capability. The image reconstruction model, based on photogrammetry, uses knowledge of the camera and light sheet locations and orientations to project two-dimensional light sheet video images into three-dimensional space. A sophisticated computer visualization package, commonly used to analyze computational fluid dynamics (CFD) results, was chosen to interactively display the reconstructed light sheet images with the numerical surface geometry for the model or aircraft under study. The photogrammetric reconstruction technique and the image processing and computer graphics techniques and equipment are described. Results of the computer-aided process applied to both a wind tunnel translating light sheet experiment and an in-flight rotating light sheet experiment are presented. The capability to compare reconstructed experimental light sheet images with CFD solutions in the same graphics environment is also demonstrated.*

## Introduction

Flow visualization techniques are important tools for the aerodynamicist. The ability to see a flow can aid in the development of heuristic flow models. One common technique used at Langley Research Center is light sheet illumination of particle-seeded flow. A single, stationary light sheet allows characteristic structures of the flow to be visualized for one slice of a three-dimensional (3-D) flow field. The recording camera is often restricted to a fixed location outside the test section for wind tunnel applications or onboard the aircraft for in-flight experiments, and it has an oblique orientation to the light sheet. Consequently, the recorded images suffer from perspective distortion that must be accounted for when making geometric measurements. Digital image processing techniques are available to extract quantitative data from light sheet images and to correct for perspective distortions (ref. 1). These techniques rely on photographing a physical grid of known geometry in the plane of the light sheet with the recording camera. Although this method is relatively simple for experiments involving stationary light sheets, it is not practical for experiments in which the light sheet moves.

Advances in the design of light sheet systems have resulted in greater flexibility of the light sheet technique. For example, capabilities now exist to control the size and the position of light sheets in real time, translate and rotate single sheets through a volume, and synchronize the sheet with pertinent flow oscillations (ref. 2). These systems offer aerodynamicists the opportunity to see multiple slices of the 3-D flow field about a model. However, the task of analyzing and interpreting the recorded two-dimensional (2-D) images is not an easy one. The ability to make accurate geometric measurements of 3-D structures in the flow field requires a more sophisticated technique than photographing a physical grid in the plane of each light sheet. Trying to form a mental image of the 3-D flow field based on viewing a sequence of 2-D slices through it is difficult. Thus, a capability for visualizing the slices as a volume of data is needed.

The purpose of this paper is to describe a computer-aided process that was developed to enhance the usefulness of 3-D light sheet flow visualization techniques. The main objective was to

reconstruct the 3-D geometric shape of the visible region illuminated by translating and rotating light sheets. The computer process combines digital image processing and computer graphics procedures and a 3-D reconstruction algorithm based on photogrammetry. This process has been applied to light sheet images generated at Langley Research Center, and it provides researchers with an enhanced analysis capability for understanding flow behavior. This paper describes the sequence of procedures that have been proven to be effective at providing quantitative geometrical position information for features of interest in the flow field and an improved qualitative analysis capability. The description of the photogrammetric reconstruction technique, the image processing and computer graphics techniques and equipment, and the results of the computer-aided process applied to both a wind tunnel and an in-flight flow visualization experiment are presented.

## Symbols

$A$	subset of pixels used to find center of brightness
$a_i$	affinity distortion terms
$B$	subset of pixels of $A$
$b_i$	coefficients of general equation of light sheet plane
$c$	camera constant corresponding to lens effective focal length
$D_i$	vectors emanating from vertices of triangle
$f_i$	input 2-D digital images
$g_i$	output 2-D digital images
$k_i$	radial distortion terms
$l$	pixel gray-level value
$M$	3 by 3 rotation matrix
$m$	horizontal scan line position of pixel
$m_{cb}$	horizontal scan line position of center of brightness
$N$	normal vector to triangle
$n$	column position of pixel
$n_{cb}$	column position of center of brightness
$n_i$	components of normal vector to triangle
$O'$	orthographic projection of object point
$P$	point within the plane of triangle
$p_i$	lens decentering distortion terms
$S$	arbitrary surface in object coordinates
$t$	parameter in parametric equations of a line in 3-D space
$V_i$	vertices of triangle
$V'_i$	orthographic projection of vertices of triangle
$X, Y, Z$	object space coordinates
$x, y, z$	image space coordinates



$x_p, y_p$	photogrammetric principal point
$\alpha$	angle of attack, deg
$\Delta x, \Delta y$	parameter set for removing biases in imaging system
$\omega, \phi, \kappa$	angles for camera orientation, deg
$\Phi$	light sheet position angle measured counterclockwise from fuselage nose, deg

Subscripts:

$C$	camera lens center
$I$	image point
$O$	object point
$S$	light sheet origin

Abbreviations:

2-D	two-dimensional
3-D	three-dimensional
ADI	analog-digital interface
ALU	arithmetic logic unit
BART	Basic Aerodynamic Research Tunnel
CFD	computational fluid dynamics
CRAMPA	Close Range Multistation Photogrammetric Adjustment
DVAL	Data Visualization and Animation Laboratory
FAST	Flow Analysis Software Toolkit
FB	frame buffer
ITI	Imaging Technologies Incorporated
RTDD	real-time digital disk
RTMP	real-time modular processor
SGI	Silicon Graphics, Incorporated
VIPS	Video Image Processing System

## Model for Image Reconstruction

The image reconstruction technique developed in this section is based on a simple form of photogrammetry. This technique replaces one of the cameras of a conventional stereo photogrammetry system with a light sheet. The reconstruction model consists of an object/image coordinate system transformation, the collinearity condition of photogrammetry, and the equation of the light sheet plane. A simple set of equations relating ideal image and object coordinates is developed in this section. The important operational procedures for determining camera calibration and the experimental geometry are described in the section entitled "Steps in Image Reconstruction."

Objects and their images are located with respect to an object  $(X, Y, Z)$  and an image  $(x, y, z)$  coordinate system, respectively. The two systems are related by a simple coordinate

transformation. The origin and the orientation of the object system are arbitrary. The origin of the image system is located at  $(X_C, Y_C, Z_C)$  in object coordinates. The orientation of the image system with respect to the object system is given by the rotation angles  $\omega, \phi, \kappa$  via the 3 by 3 rotation matrix  $\mathbf{M} = (m_{i,j})$  defined as

$$\mathbf{M} = \begin{bmatrix} \cos \kappa & \sin \kappa & 0 \\ -\sin \kappa & \cos \kappa & 0 \\ 0 & 0 & 1 \end{bmatrix} \begin{bmatrix} \cos \phi & 0 & \sin \phi \\ 0 & 1 & 0 \\ -\sin \phi & 0 & \cos \phi \end{bmatrix} \begin{bmatrix} 1 & 0 & 0 \\ 0 & \cos \omega & \sin \omega \\ 0 & -\sin \omega & \cos \omega \end{bmatrix} \quad (1)$$

The rotation angles are defined as positive for counterclockwise rotation when observed from the positive end of an axis looking toward the origin. The coordinate transformation from image to object system is therefore given by

$$\begin{bmatrix} X \\ Y \\ Z \end{bmatrix} = \begin{bmatrix} m_{11} & m_{12} & m_{13} \\ m_{21} & m_{22} & m_{23} \\ m_{31} & m_{32} & m_{33} \end{bmatrix}^T \begin{bmatrix} x \\ y \\ z \end{bmatrix} + \begin{bmatrix} X_C \\ Y_C \\ Z_C \end{bmatrix} \quad (2)$$

A typical reconstruction geometry is illustrated in figure 1. Note that the camera lens is located at the origin of the image coordinate system, that the camera points along the negative  $z$ -axis, and that the  $x$ - and  $y$ -axes exit to the right and the top of the camera lens, respectively. The collinearity condition of photogrammetry requires that an object, its image, and the lens center lie on a line, as shown in figure 1. The object is located at  $(X_O, Y_O, Z_O)$  in object coordinates, and its image is located at  $(x_I, y_I, c)$  in image coordinates, where  $c$  is the effective focal length of the lens that locates the image plane. A set of parametric equations for this line can be written as

$$\left. \begin{aligned} X &= X_C + (X_I - X_C)t \\ Y &= Y_C + (Y_I - Y_C)t \\ Z &= Z_C + (Z_I - Z_C)t \end{aligned} \right\} \quad (3)$$

where  $(X_I, Y_I, Z_I)$  are the object coordinates of the image point  $(x_I, y_I, c)$ , which are given by equation (2). These equations can represent any point  $(X, Y, Z)$  on the line. Because the object point also lies in the plane of the light sheet, its coordinates are given by the intersection of the line and an equation representing the light sheet plane. This intersection process is called triangulation. The origin of the light sheet is located at  $(X_S, Y_S, Z_S)$ , as shown in figure 1. In general, the light sheet plane equation can be written in the form

$$b_1 X + b_2 Y + b_3 Z + b_4 = 0 \quad (4)$$

By substituting equation (3) into equation (4),  $t$  is determined to be

$$t = \frac{b_1 X_C + b_2 Y_C + b_3 Z_C + b_4}{b_1 (X_C - X_I) + b_2 (Y_C - Y_I) + b_3 (Z_C - Z_I)} \quad (5)$$

By substituting this value for  $t$  back into equation (3), the unique object coordinates  $(X_O, Y_O, Z_O)$  can be evaluated.

## Steps in Image Reconstruction

The model described above is ideal because the camera was assumed to provide a distortion-free image and the location of the camera and of the light sheet are assumed known. However,

cameras (especially short focal length cameras) can exhibit considerable image plane distortion, and the location and the orientation of the camera and the light sheet need to be determined experimentally. The following three sections discuss these steps.

### Imaging System Calibration

Video imaging systems suffer from a wide variety of nonideal behavior. With the recent proliferation of commercial charge-coupled device (CCD) cameras, a significant step has been made in maintaining the stability of the sensor elements. However, CCD cameras are not a panacea that ensures worry-free image quality and measurement capability. Although most of the time-dependent effects associated with reticon tube cameras have been eliminated, video systems still fundamentally use analog technology and require extensive calibration.

Fortunately, the photogrammetric community has developed sophisticated procedures and algorithms for calibrating cameras over the past few decades. Application of these techniques to video systems (refs. 3 and 4) allows reduction of systematic image plane errors to residual levels of approximately  $0.5 \mu\text{m}$ . By comparison, an uncalibrated imaging system can easily have image plane errors on the order of  $50 \mu\text{m}$  or more.

It is important to realize that the entire video system, not just the camera, should be included in the calibration procedure. It is not uncommon for a video imaging system to include video camera, VCR, time-base corrector, intermediate storage onto an optical videodisc, and video frame digitizer. Each device presents an opportunity for added systematic bias and overall image-quality degradation.

The equations of photogrammetry that model the projection of object coordinates  $(X, Y, Z)$  to refined image plane coordinates  $(x, y)$  of a camera are (ref. 5)

$$\left. \begin{aligned} x &= x' + \Delta x = x_p - c \left[ \frac{m_{11}(X_C - X) + m_{12}(Y_C - Y) + m_{13}(Z_C - Z)}{m_{31}(X_C - X) + m_{32}(Y_C - Y) + m_{33}(Z_C - Z)} \right] \\ y &= y' + \Delta y = y_p - c \left[ \frac{m_{21}(X_C - X) + m_{22}(Y_C - Y) + m_{23}(Z_C - Z)}{m_{31}(X_C - X) + m_{32}(Y_C - Y) + m_{33}(Z_C - Z)} \right] \end{aligned} \right\} \quad (6)$$

The point  $(x', y')$  is the measured image plane location of an object point,  $(x_p, y_p)$  is the photogrammetric principal point, and the  $\Delta x$  and  $\Delta y$  terms represent functions for modeling the distortions of the imaging system. A commonly used set of functions for  $\Delta x$  and  $\Delta y$  is

$$\left. \begin{aligned} \Delta x &= \bar{x} \left( k_1 r^2 + k_2 r^4 + k_3 r^6 \right) + p_1 \left( r^2 + 2\bar{x}^2 \right) + 2p_2 \bar{x}\bar{y} \\ \Delta y &= \bar{y} \left( k_1 r^2 + k_2 r^4 + k_3 r^6 \right) + 2p_1 \bar{x}\bar{y} + p_2 \left( r^2 + 2\bar{y}^2 \right) + a_1 \bar{x} + a_2 \bar{y} \end{aligned} \right\} \quad (7)$$

where  $r^2 = (x - x_p)^2 + (y - y_p)^2 \equiv \bar{x}^2 + \bar{y}^2$ , and  $k_i$ ,  $p_i$ , and  $a_i$  represent radial, lens decentering, and affinity distortion terms, respectively.

A set of  $n$  independently and accurately located calibration targets are imaged from  $m$  points of view, called stations, with the same camera. Figure 2 shows an image of a typical calibration target plate from one station. Each target contributes two equations per station for a total of  $2mn$  equations. Each station contributes six unknown exterior orientation parameters  $(\omega, \phi, \kappa, X_C, Y_C, Z_C)$ , which yield  $6m$  unknowns. In addition, there are 10 unknown interior orientation parameters  $(x_p, y_p, c, k_1, k_2, k_3, p_1, p_2, a_1, \text{ and } a_2)$ , for a total of  $6m + 10$  unknowns. If 100 calibration targets and 8 stations are used, this results in 1600 equations and 58 unknowns. The large overdetermined system of nonlinear equations is solved iteratively for all the unknowns

in what is called a bundle adjustment. The software used to obtain the solution, CRAMPA (Close Range Multistation Photogrammetric Adjustment), is a commercially available suite of C programs (ref. 6). The CRAMPA software is a highly specialized code utilizing the most recent results of research in close range photogrammetry. Nine of the 10 interior orientation parameters, excluding  $c$ , are used to remove the systematic biases in subsequent image plane measurements. The effective focal length  $c$  determines the scale of the imaging system and is also important.

Every light sheet image must have a valid set of interior orientation parameters to achieve the maximum potential accuracy. Because the calibration images are usually taken at a different time (often days apart) than the light sheet images, it is important to take precautions against altering the imaging system in the interim. Any changes in the imaging system, such as using a different VCR or digitizer board or refocusing the camera, compromise the calibration. In situations in which the calibration has been compromised, one must recalibrate or tolerate greatly reduced accuracy.

### **Determining Camera Orientation**

After the camera has been properly placed to obtain images of the light sheet, images of another set of independently and accurately known object points, called control points, are obtained to establish the location and the orientation of the camera. The measured control point image locations are then corrected with the calibration parameters, and equation (6) is solved for each control point, excluding the  $\Delta$  terms. This time, the equations are solved only for the exterior orientation parameters ( $\omega, \phi, \kappa, X_C, Y_C, Z_C$ ). A minimum of three control points is required, but more should be used if possible. This is a standard photogrammetric procedure called space resection.

Every light sheet image must have a valid set of exterior orientation parameters associated with it. This set of parameters may change frequently during data acquisition because of movement of the camera or the control points. In these cases, a systematic procedure for determining the parameters for each light sheet image must be devised.

### **Determining Light Sheet Orientation**

The technique for determining the light sheet orientation parameters  $b_i$  differs for the experiments described below, and no general analytic method has yet been incorporated. The light sheet parameters can be fixed by alignment procedures for simple geometries. In other cases, transit measurements with respect to the control points must suffice. Until analytic techniques are incorporated, the light sheet parameters will limit the system accuracy.

Every light sheet image must have a valid set of light sheet parameters associated with it. This set of parameters may change frequently during data acquisition because of movement of the light sheet or the control points. In these cases, a systematic procedure for determining the parameters for each light sheet image must be devised.

## **Examples of Translating and Rotating Light Sheet Experiments**

### **Wind Tunnel Example**

A laser light sheet flow visualization experiment was performed in a wind tunnel by researchers investigating the relationship between buffeting and the vortical flow field over a wing (ref. 7). The investigation was conducted in the Basic Aerodynamic Research Tunnel (BART) at Langley. The BART is a test facility dedicated to code validation (ref. 8). Off-body flow visualization was obtained from laser light sheets illuminating smoke that was entrained in the flow. The model,

shown in figure 3, consisted of twin vertical tails placed on tail support booms that were aft of a  $76^\circ$  flat delta wing. The model was tested at angles of attack  $\alpha$  of  $20^\circ$  and  $30^\circ$ .

An illustration of the BART experimental geometry for  $\alpha = 20^\circ$  is shown in figure 4. A stationary video camera mounted above the glass ceiling of the test section and forward of the model was used to record the images. The light sheet, which was mounted on a traversing mechanism above the test section, was directed downward onto the model. The beginning and ending light sheet locations are represented in figure 4 as grids. The 3-D region over which flow-field data were obtained during the experiment is bounded by the camera field of view and the beginning and ending light sheet planes. The camera sensor array, which is represented by grid lines in the image plane, projects through the lens center to grid lines in the light sheet planes.

To obtain the position and the orientation of the recording camera via the space resection procedure, a minimum of three control points is required. These points were conveniently obtained for this experiment by using the three sharp corners at the nose and wing tips of the model. The locations of these corners were obtained from model construction schematics, and they were assumed to be accurate. Figure 5(a) shows the locations of the corners in the video image, and figure 5(b) shows a typical light sheet image. The object coordinate system was defined with the origin at the model nose and the wing tips in the  $X$ - $Y$  plane, as shown in figure 6. The  $X$  coordinates of the wing tips were defined to be 100-percent model chord with the  $Y$  coordinates scaled appropriately.

Data for the light sheet plane location are required for the reconstruction process. The task of accurate light sheet placement was simplified for this experiment by the flat triangular model shape. The sheet was manually aligned so that both the wing tips were in the light sheet and a flat mirror placed on the model surface would reflect the light sheet back to its source. This alignment procedure ensured that the light sheet was parallel to the  $Y$ - $Z$  plane. The traversing mechanism was used during the tests to position the light sheet along the  $X$ -axis from 20- to 160-percent model chord, in 10-percent increments. These positions are illustrated in figure 6. The equations for the light sheet planes are then given by  $X = 0.2, X = 0.3, \dots, X = 1.6$ . These equations correspond to equation (4) with  $b_1 = -1.0$ ,  $b_2 = 0$ ,  $b_3 = 0$ , and  $b_4 = 0.2, 0.3, \dots, 1.6$ . A typical light sheet image for this experiment is shown in figure 5(b). Although the geometric reconstruction of the light sheet plane has been discussed in detail, the flow features revealed by scattered light and recorded as gray-level variations in the image have not yet been addressed. The process of assigning a gray-level value to each object point location based on the scattered light intensity of the corresponding image point will be described in the section entitled "Computer Visualization Process."

### In-Flight Example

An in-flight flow visualization experiment was performed by researchers investigating the origination of the vortex system and multiple vortices over the wing of the F-106B aircraft (ref. 9). Off-surface flow visualization was obtained by illuminating propylene-glycol vapor entrained in the flow with a rotating light sheet. A photograph of the F-106B aircraft indicating the vapor-screen components is shown in figure 7. (This figure shows a removable leading-edge flap attached to the wing that was not used for the flight data presented in this paper.) The propylene-glycol vapor was introduced into the flow through a probe located underneath the left wing near the leading edge. Two video cameras, one mounted on top of the fuselage in front of the light sheet housing and the other mounted on the left inlet, were used to record the images. An illustration of the F-106B aircraft experimental geometry for the top camera is shown in figure 8. This illustration is similar to the one shown for the BART experiment except that the camera sensor array is omitted for clarity. The light sheet was emitted through a narrow

rotating slit located on top of the fuselage. The inlet camera had a view of the apex region and the upper wing surface, and the top camera had a view more aft along the wing upper surface. The rotating light sheet swept a range of angles from  $40^\circ$  to  $125^\circ$  aft of the aircraft centerline, and it remained perpendicular to the wing upper surface. The light sheet angle during sweeps was recorded. The 3-D region over which flow-field data were obtained is the intersection of the camera field of view and the area illuminated by the rotating light sheet. The object coordinate system shown was adopted to be compatible with other measurements performed on the aircraft. The techniques used to locate the control points and light sheet are described below.

Because no conveniently identifiable wing features were available, such as the sharp corners on the BART delta wing, the control points had to be manufactured. A video image of the control points is shown in figure 9(a), and a vapor screen image is shown in figure 9(b). The control points were circular pieces of cardboard centered as close as possible on the intersections of wing spars and ribs. The  $X$  and  $Y$  coordinates of the spars and ribs were documented in the original F-106B aircraft construction schematics. The  $Z$  values were measured by a scale from a level line.

The light sheet was designed to rotate about a line parallel to the  $Z$ -axis. The measured location of the light sheet origin was  $X_S = 438.7$  in.,  $Y_S = 0.4$  in., and  $Z_S = 51.5$  in., as shown in figure 10. The aircraft instrumentation system provided the rotation angle  $\Phi$  measured from the nose of the aircraft. The equation of the light sheet, as a function of  $\Phi$ , is given by

$$\tan \Phi = \frac{(Y - Y_S)}{(X - X_S)} \quad (8)$$

and equivalently in the form of equation (4) as

$$(\tan \Phi)X + (-1)Y + (0)Z + (Y_S - X_S \tan \Phi) = 0 \quad (9)$$

The videotape recording of the in-flight experiment contains the primary data (i.e., the vapor-scattered light from the rotating light sheets). (See fig. 9.) A typical image, representing one slice through the 3-D flow-field, is shown in figure 9(b). One factor that makes this image difficult to analyze is that the outline of the wing upper surface is barely visible. The light sheet footprint (i.e., the intersection of the light sheet with the wing upper surface) produced the most reflection; therefore, it appears as the brightest region in the images. The footprint provides an indication of the light sheet position when examining the 2-D images.

## Computer Visualization Process

The computer visualization process is a combination of digital image processing techniques for digitizing, enhancing, and analyzing sequences of experimental images recorded on videotape and interactive computer graphics for displaying and analyzing the reconstructed image data. All visual data analysis was performed in the Data Visualization and Animation Laboratory (DVAL) at Langley Research Center. This laboratory provides advanced visualization tools on an integrated system of high-performance graphics workstations and digital image processing equipment. Current DVAL resources include Sun Microsystems, Incorporated, and Silicon Graphics, Incorporated (SGI) workstations for performing interactive computer graphics, high-quality image rendering, advanced animations, and image analysis, and a Video Image Processing System (VIPS) for performing video-rate image acquisition, processing, and storage. The VIPS is a combination of hardware and software designed to provide a specialized capability for applying enhancements at video rates to sequences of wind tunnel or in-flight images recorded on videotape.

The overall computer visualization process is illustrated in figure 11. Videotape frames were digitized and processed on the VIPS. The digital images were then analyzed on the Sun computer to extract vortex core locations. The images and the core locations were subsequently transferred to an SGI workstation where the triangulation software was executed to map image pixels into 3-D space. The camera and light sheet parameters are necessary inputs to the triangulation software. The Flow Analysis Software Toolkit (FAST) (ref. 10) on the SGI was used to interactively display the 3-D image data and the numerical surface geometry of the model.

### Digitizing and Processing Videotape

In the two examples described above, the visual record of the light sheet flow visualization experiment is a standard S-VHS videotape. In addition, a set of calibration images (see the section entitled "Imaging System Calibration") is also recorded on videotape. Prior to image reconstruction, these analog video signals must be converted to digital images. The VIPS, composed of a series 150 modular image processing subsystem from Imaging Technologies Incorporated (ITI) and a real-time digital disk (RTDD) subsystem from Storage Concepts, Incorporated, that was interfaced to a Sun computer, was used to digitize, process, and store select frames from the raw video footage of the flow visualization experiments. The block diagram in figure 12 illustrates the image processing pipeline configuration of the modules within the series 150 subsystem and the interface to the RTDD subsystem. The analog-digital interface (ADI) converts the analog video signal into a 2-D array of numbers that can be passed sequentially through the pipeline to the other modules in the subsystem. For each frame of video, the ADI divides 480 of the active horizontal video lines into 512 samples, which are known as pixels. Each pixel location is assigned an integer gray-level value between 0 and 255; this value corresponds to the brightness of the image at that location. The resulting  $512 \times 480 \times 8$  bit digital images are passed through the pipeline to other modules in the pipeline where additional processing may be performed. The real-time modular processor (RTMP) is the first module in the pipeline, followed by the arithmetic logic unit (ALU), and finally the frame buffer (FB). Pixels are processed through the pipeline at video rates (30 frames per sec). The RTDD is capable of storing approximately 8 min of full-frame digital image data. The software interface is the VISILOG image processing software from Noesis Vision, Incorporated.

During the BART experiment, the light sheet was positioned at 15 different stations along the model; these locations range from a 20-percent model chord to a 160-percent model chord. (See fig. 6.) Approximately 20 sec of video was recorded for each light sheet station. The ITI subsystem pipeline processed the digital images coming from the ADI with a pointwise recursive digital filter of the form

$$g_i = af_i + (1 - a)g_{i-1} \quad (10)$$

where  $f_i$  and  $g_i$  are the input and output images, respectively, and  $0 < a < 1$ . This temporal digital filter is commonly used in signal processing (ref. 11) to smooth digital data. A weight of  $a = 0.25$  was selected with the goal of removing noise in the images without significantly altering temporal information. The first input image was  $f_0$ , and an image of all zeros was used as the initial value for  $g_{-1}$ . The resulting time-filtered digital images were stored on the RTDD. The processed images were then played back for inspection from the RTDD at speeds less than video rates. The researcher selected one representative image for each light sheet station based on subjective image quality. The images shown in figure 5 are two examples of images digitized and processed on the ITI subsystem.

For the in-flight experiment with the F-106B aircraft, the researcher viewed the videotape in advance and selected specific frames to be digitized. Frames of interest were identified by the

visual time code appearing on each video frame. No processing was performed on these images prior to image reconstruction.

### Extracting Vortex Core Locations in 2-D Digital Images

Once the light sheet images have been digitized, interactive image analysis techniques can be applied to extract quantitative information, such as vortex core locations. The BART light sheet image at station  $X = 1.1$  will be used as an example. An enlarged gray-scale image of the port side vortex is shown in figure 13(a). The vortex core appears as a dark interior region that is void of seeding particles. The location of the vortex core centroid is determined by finding the center of mass of the contrast reversed pixels within these dark regions. A better terminology might be center of brightness because a brightness value is more commonly associated with pixels.

The center of brightness computation is restricted to a subset of pixels that makes up the dark interior region of the vortex. This subset is determined by using a sequence of simple steps. First, the researcher specifies an initial estimate of the vortex core location by selecting a single pixel somewhere inside the dark interior region of the vortex. If the image is thought of as a brightness surface, in which the height of each pixel is determined by its gray-level value or brightness, then the initial guess pixel serves as the input for a technique that finds the valley (the dark area) of the region surrounding this pixel. This process is analogous to letting a ball roll down a hill (the bright area). The output pixel location replaces the researcher's initial guess and serves as the input for a technique that searches for the ridge of the hill. The result is a closed boundary (shown in fig. 13(b)) which defines the subset A of pixels to be considered for use in the center of brightness computation. Pseudocolor, an assignment of colors to gray-level values, is used in the figure to contrast variations within the vortex core. Once A has been determined, B (a subset of A) is defined by applying a gray-level threshold to the pixels in A. Subset B, which is shown in figure 13(c) as an entirely black region, represents the pixels in subset A with a gray-level value below the chosen threshold. Let  $N$  be the number of pixels in B and  $l_1, l_2, \dots, l_N$  be the gray-level values corresponding to the horizontal scan line and column positions  $(m_1, n_1), (m_2, n_2), \dots, (m_N, n_N)$  of the pixels in B. Then, the center of brightness of the contrast reversed pixels in B is determined by

$$\left. \begin{aligned} m_{cb} &= \frac{\sum_{i=1}^N m_i(255 - l_i)}{\sum_{i=1}^N (255 - l_i)} \\ n_{cb} &= \frac{\sum_{i=1}^N n_i(255 - l_i)}{\sum_{i=1}^N (255 - l_i)} \end{aligned} \right\} \quad (11)$$

The  $m_{cb}$  and  $n_{cb}$  coordinates were chosen as the vortex core location. The crosshair in figure 13(c) indicates the computed pixel location of the vortex core.

### Interactive Display of Reconstructed Images and Numerical Surface Geometry

The photogrammetric reconstruction of a single  $512 \times 480$  digital image requires 3.75 Mb of storage space. The total storage requirement depends on the number of light sheet planes to be analyzed and the additional storage required for the numerical surface geometry of the model. Typically, anywhere between 10 and 15 images per test condition were studied for the two experiments discussed above. A sophisticated visualization package is required to interactively display experimental data sets of this magnitude. The package currently used for this work is the Flow Analysis Software Toolkit (FAST) running on the SGI workstation.

The FAST was originally developed as a postprocessing graphics environment for viewing and analyzing computational fluid dynamics (CFD) results. A grid file and matching function



file are read into FAST. The grid file contains the 3-D coordinates of a finite number of points in the flow field, and the function file contains a set of scalar values associated with each grid point. Experimental data can be expressed in a similar manner. The triangulation software produces the grid file by computing 3-D object coordinates for each pixel in a set of 2-D video images. The digitization process produces the function file containing pixel gray-level values. These two files can be generated and input into FAST to interactively visualize any desired test condition.

Many features of the highly interactive FAST environment are useful for analyzing the experimental data sets. Figure 14 shows several user interface windows that appear on the SGI display during a FAST session. The delta wing numerical surface geometry, the reconstructed light sheet images, and the vortex core paths are displayed in the *Active View Window*. To create this display, grid files for the delta wing, twin tails, light sheet stations, and vortex core locations are selected for data input. Also, the light sheet intensities corresponding to the light sheet grid are selected. Pseudocolor is used to display the light sheet intensities. A range of low intensities (from 0 to 20) are clipped (i.e., not displayed) by using a thresholding option in FAST, thus allowing only the vortex structure to be seen. Also, object points with  $Z$  values less than 0 are not displayed, which eliminates unimportant data below the wing. The entire scene can be rotated, translated, and zoomed in and out with the interactive viewing controls. A data probe and a probe readout can be used to examine the 3-D coordinates of any grid point in any of the scene objects. In figure 14, the probe is being used to look at the  $X$ ,  $Y$ , and  $Z$  values for the port side vortex core at light sheet station  $X = 0.7$ .

The entire scene shown in the *Active View Window* in figure 14 is created in a progression, as shown in figures 15(a) to (f). First, the numerical surface geometry of the delta wing and the vertical twin tails is input and displayed with grid lines (fig. 15(a)). The model can also be rendered as a smooth shaded surface to provide a more realistic view (fig. 15(b)). Figure 15(c) shows the smooth shaded surface with the light sheet grid for station  $X = 1.1$ . The function values at each grid point, in this case image intensities, are interpolated to produce a smoothly varying function on the light sheet plane, as shown in figure 15(d). Function values below a specified value are clipped, and every other light sheet station is displayed in figure 15(e). Figure 15(f) shows a continuous vortex core path by connecting the vortex core points extracted for each light sheet station with straight lines. A similar progression for the port wing of the F-106B aircraft is shown in figures 16(a) to (f). The entire F-106B aircraft can be displayed in FAST with selected light sheet images, as shown in figure 17.

The objects in a scene can be rotated and viewed from any angle. Figure 18 shows a top and a side view of the delta wing with just the reconstructed vortex core points connected by straight lines. The top view gives insight into the distance the core path is from the leading edge, whereas the side view provides insight into the height of the vortex core above the delta wing surface.

An advantage of using FAST to analyze the experimental data sets is the capability to perform visual comparisons with CFD data sets. Figure 19 shows the delta wing with experimental data on the port side and the computational stagnation pressure contours on the starboard side (ref. 12). There is no physical correspondence between the colors used to represent the light intensity in the experimental images and the colors used to represent the computational stagnation pressure contours. Nevertheless, the side-by-side comparison is useful for a visual comparison of vortex system features, which are indicated by the computed yellow particle traces on the computational side and a white line on the experimental side.

## Extension for On-Surface Mapping

A powerful extension to this technique was developed to reconstruct images of flow phenomena confined to the surface of an airfoil, such as the oil-flow image in figure 20(a). This image was

acquired during a daylight flight of the F-106B aircraft after applying an oil mixture to the leading-edge region of the left wing. The oil patterns on the wing surface were acquired by the same camera used to record vapor-screen images from the top of the fuselage.

The same coordinate system transformation and collinearity condition expressed in equations (1) to (3) are assumed here, and only equations (4) and (5), which are specific for a planar surface, must be modified or replaced. In theory, the surface  $S$  of interest can be defined implicitly in object coordinates by

$$S(X, Y, Z) = 0 \quad (12)$$

If  $(X_I, Y_I, Z_I)$  is the image point of an object confined to this surface, then the coordinates of the object can be determined by intersecting the line containing the lens center and the image point (eq. (3)) with the equation of the surface to obtain

$$S(X_C + (X_I - X_C)t, Y_C + (Y_I - Y_C)t, Z_C + (Z_I - Z_C)t) = 0 \quad (13)$$

which must be solved for  $t$ . (This is a problem similar to ray tracing in computer graphics applications.) If  $S$  is a quadric surface, for example, finding the roots of equation (13) is equivalent to solving a quadratic equation.

In general, the solutions to equation (13) may be real or complex. If only complex values for  $t$  result, then the object point corresponding to the image point  $(X_I, Y_I, Z_I)$  does not lie on  $S$ . Furthermore, negative values for  $t$  indicate points on  $S$  that lie behind the image plane of the camera; therefore, these points cannot be object points. Thus, only positive, real solutions to equation (13) represent valid object points within the field of view of the camera. If more than one such solution is found, then several points on  $S$  lie along the line of sight, but the point closest to the camera is assumed to obscure the others. Therefore, although equation (13) may have several solutions for  $t$ , the smallest positive real value for  $t$  is selected to represent the object point. The final coordinates  $(X_O, Y_O, Z_O)$  can then be directly determined with equation (3).

In practice, equation (12) is difficult to derive, and equation (13) is even more difficult to solve except for surfaces described by low-order polynomials (such as spherical or parabolic surfaces). Therefore, an airfoil surface is often approximated by a mesh of quadrilaterals or triangles; this mesh is commonly referred to in CFD applications as a structured or an unstructured grid, respectively. The numerical surface geometry shown in figure 20(b), for example, is composed of quadrilaterals, and it was used to approximate the wing surface of the F-106B aircraft. Each quadrilateral can be further subdivided into two triangles. Thus, the problem of mapping an image onto an arbitrary surface can be approximated by mapping that image onto a mesh of triangles.

To determine if a given triangle in the mesh contains the object corresponding to a given image point  $(X_I, Y_I, Z_I)$ , the equation of the plane containing the triangle must first be derived. Recall that a normal vector  $\mathbf{N}$  to any triangle in object coordinates with vertices  $\mathbf{V}_0$ ,  $\mathbf{V}_1$ , and  $\mathbf{V}_2$ , where

$$\mathbf{N} = \begin{bmatrix} n_1 \\ n_2 \\ n_3 \end{bmatrix} \quad \mathbf{V}_0 = \begin{bmatrix} X_0 \\ Y_0 \\ Z_0 \end{bmatrix} \quad \mathbf{V}_1 = \begin{bmatrix} X_1 \\ Y_1 \\ Z_1 \end{bmatrix} \quad \mathbf{V}_2 = \begin{bmatrix} X_2 \\ Y_2 \\ Z_2 \end{bmatrix} \quad (14)$$

can be derived by using the cross product of the vectors  $\mathbf{V}_1 - \mathbf{V}_0$  and  $\mathbf{V}_2 - \mathbf{V}_0$ :

$$\mathbf{N} = (\mathbf{V}_1 - \mathbf{V}_0) \times (\mathbf{V}_2 - \mathbf{V}_0) = \begin{bmatrix} X_1 - X_0 \\ Y_1 - Y_0 \\ Z_1 - Z_0 \end{bmatrix} \times \begin{bmatrix} X_2 - X_0 \\ Y_2 - Y_0 \\ Z_2 - Z_0 \end{bmatrix} \quad (15)$$

$$\mathbf{N} = \begin{bmatrix} n_1 \\ n_2 \\ n_3 \end{bmatrix} = \begin{bmatrix} (Y_1 - Y_0)(Z_2 - Z_0) - (Y_2 - Y_0)(Z_1 - Z_0) \\ (X_2 - X_0)(Z_1 - Z_0) - (X_1 - X_0)(Z_2 - Z_0) \\ (X_1 - X_0)(Y_2 - Y_0) - (X_2 - X_0)(Y_1 - Y_0) \end{bmatrix}$$

Furthermore, if  $\mathbf{P} = \begin{bmatrix} X \\ Y \\ Z \end{bmatrix}$  is any point within the plane containing the triangle, then  $\mathbf{N}$  and  $\mathbf{P} - \mathbf{V}_0$  are orthogonal, and their dot product must be zero such that

$$\mathbf{N} \cdot (\mathbf{P} - \mathbf{V}_0) = \begin{bmatrix} n_1 \\ n_2 \\ n_3 \end{bmatrix} \cdot \begin{bmatrix} X - X_0 \\ Y - Y_0 \\ Z - Z_0 \end{bmatrix} = n_1(X - X_0) + n_2(Y - Y_0) + n_3(Z - Z_0) = 0 \quad (16)$$

Therefore, the equation of the plane containing this triangle is

$$n_1X + n_2Y + n_3Z - (n_1X_0 + n_2Y_0 + n_3Z_0) = 0 \quad (17)$$

Or, in terms of equation (4),  $b_1 = n_1$ ,  $b_2 = n_2$ ,  $b_3 = n_3$ , and  $b_4 = -(n_1X_0 + n_2Y_0 + n_3Z_0)$

The point  $\mathbf{O} = \begin{bmatrix} X_O \\ Y_O \\ Z_O \end{bmatrix}$ , at which the line of sight intersects the plane containing the triangle, is illustrated in figure 21(a). The object coordinates of point  $\mathbf{O}$  can be derived by using equations (3) and (5). To determine if this point is actually within the triangle, however, an orthographic projection of both  $\mathbf{O}$  and the vertices  $\mathbf{V}_0$ ,  $\mathbf{V}_1$ , and  $\mathbf{V}_2$  is performed to produce  $\mathbf{O}'$ ,  $\mathbf{V}'_0$ ,  $\mathbf{V}'_1$ , and  $\mathbf{V}'_2$ . If these points are projected into the  $X$ - $Y$  plane, for example, then the  $Z$  coordinate is dropped and

$$\mathbf{O}' = \begin{bmatrix} X_O \\ Y_O \end{bmatrix} \quad \mathbf{V}'_0 = \begin{bmatrix} X_0 \\ Y_0 \end{bmatrix} \quad \mathbf{V}'_1 = \begin{bmatrix} X_1 \\ Y_1 \end{bmatrix} \quad \mathbf{V}'_2 = \begin{bmatrix} X_2 \\ Y_2 \end{bmatrix} \quad (18)$$

Finally, if  $\mathbf{D}_0$ ,  $\mathbf{D}_1$ , and  $\mathbf{D}_2$  are defined as shown in figure 21(b) as

$$\begin{aligned} \mathbf{D}_0 &= (\mathbf{O}' - \mathbf{V}'_0) \times (\mathbf{V}'_1 - \mathbf{V}'_0) \\ \mathbf{D}_1 &= (\mathbf{O}' - \mathbf{V}'_1) \times (\mathbf{V}'_2 - \mathbf{V}'_1) \\ \mathbf{D}_2 &= (\mathbf{O}' - \mathbf{V}'_2) \times (\mathbf{V}'_0 - \mathbf{V}'_2) \end{aligned} \quad (19)$$

then  $\mathbf{D}_0$ ,  $\mathbf{D}_1$ , and  $\mathbf{D}_2$  have the same sign if and only if  $\mathbf{O}$  is within the triangle.

This technique to map images onto a triangular mesh was successfully applied to reconstruct the oil-flow images that were acquired from the F-106B aircraft. The numerical surface geometry of figure 20(b) was used as the basis for the triangular mesh, and the camera parameters of interior and exterior orientation from the light sheet reconstruction were used as well. Figure 22(a) shows a reconstructed oil-flow result that was interactively rendered with the

FAST package. This information was easily combined in FAST with data acquired by using the light sheet to produce figure 22(b). The capability to combine off-surface and on-surface flow visualization data into the same 3-D interactive visualization environment provides the aerodynamicist with an even more powerful quantitative and qualitative analysis tool.

With complete knowledge of the interior and exterior camera orientation parameters and a geometric description of the airfoil surface, this technique could be applied equally well to images of on-surface flow acquired from a variety of airfoils with substances such as colored water, liquid crystals, and pressure-sensitive paints.

## Conclusions

Research has demonstrated that the computer-aided image reconstruction technique can be effectively applied to research projects with moving light sheets to visualize three-dimensional (3-D) flow fields. The technique provides researchers with a 3-D quantitative and qualitative analysis capability for two-dimensional (2-D) light sheet images recorded on videotape; previously these light sheet images were difficult to evaluate. An extension of this technique enables on-surface flow visualization images, such as oil flows, to also be mapped onto the surface of models. Once the maps are represented in 3-D, they can be observed from any viewpoint, thus freeing the researcher from the original camera view. This technique shows promise in aiding the visual comparison of experimental images and computational fluid dynamics (CFD) solutions because experimental data can now be visualized with the same computer graphics environment, Flow Analysis Software Toolkit (FAST), which is commonly used for analyzing and interpreting CFD solutions. Graphics environments such as FAST allow the object space coordinates locations and function values of image and grid points to be examined interactively. In addition to a 3-D visualization tool, the technique provides mathematically precise quantitative information about locations and structures of vortex systems, thus allowing information (such as the distance from vortex core locations to the wing leading edge) to be easily derived and extracted.

NASA Langley Research Center  
Hampton, VA 23681-0001  
February 28, 1994

## References

1. O'Hare, Joe E.: Digital Image Analysis for Aerodynamic Testing. *International Instrumentation Symposium—27th Proceedings*, Inst. Soc. America, Apr. 1981, pp. 131–136.
2. Rhodes, David B.; Franke, John M.; Jones, Stephen B.; and Leighty, Bradley D.: *A Twin-Mirrored Galvanometer Laser Light Sheet Generator*. NASA TM-100587, 1988.
3. Wong, Kam W.: Geometric Distortions in Television Imageries. *Photogramm. Eng.*, vol. 35, no. 5, 1969, pp. 493–500.
4. El-Hakim, S. F.: Real-Time Image Metrology With CCD Cameras. *Photogramm. Eng. & Remote Sens.*, vol. 52, no. 11, Nov. 1986, pp. 1757–1766.
5. Karara, H. M., ed.: *Non-Topographic Photogrammetry*, Second ed. American Soc. for Photogrammetry and Remote Sensing, 1989.
6. CRAMPA—*Close Range Multistation Photogrammetric Adjustment Reference Guide*. Version 1.1, Geometric Software (Coburg, Austral.), May 1993.
7. Washburn, Anthony E.; Jenkins, Luther N.; and Ferman, Marty A.: Experimental Investigation of Vortex-Fin Interaction. AIAA-93-0050, Jan. 1993.
8. Sellers, William L., III; and Kjelgaard, Scott O.: The Basic Aerodynamics Research Tunnel—A Facility Dedicated to Code Validation. AIAA-88-1997, May 1988.
9. Lamar, John E.; Brandon, Jay; Stacy, Kathryn; Johnson, Thomas D., Jr.; Severance, Kurt; and Childers, Brooks A.: *Leading-Edge Vortex System Details Obtained on F-106B Aircraft Using a Rotating Vapor-Screen and Surface Techniques*. NASA TP-3374, 1993.
10. Walatka, Pamela P.; Culcas, Jean; McCabe, R. Kevin; Plessel, Todd; and Potter, Rick: *FAST 1.0 User Guide*. RND-92-015, NASA Ames Research Center, Nov. 1992.
11. Hamming, R. W.: *Digital Filters*, Second ed. Prentice-Hall, Inc., 1983.
12. Krist, Sherrie L.; Washburn, Anthony E.; and Visser, Kenneth D.: A Computational and Experimental Investigation of a Delta Wing With Vertical Tails. AIAA-93-3009, July 1993.

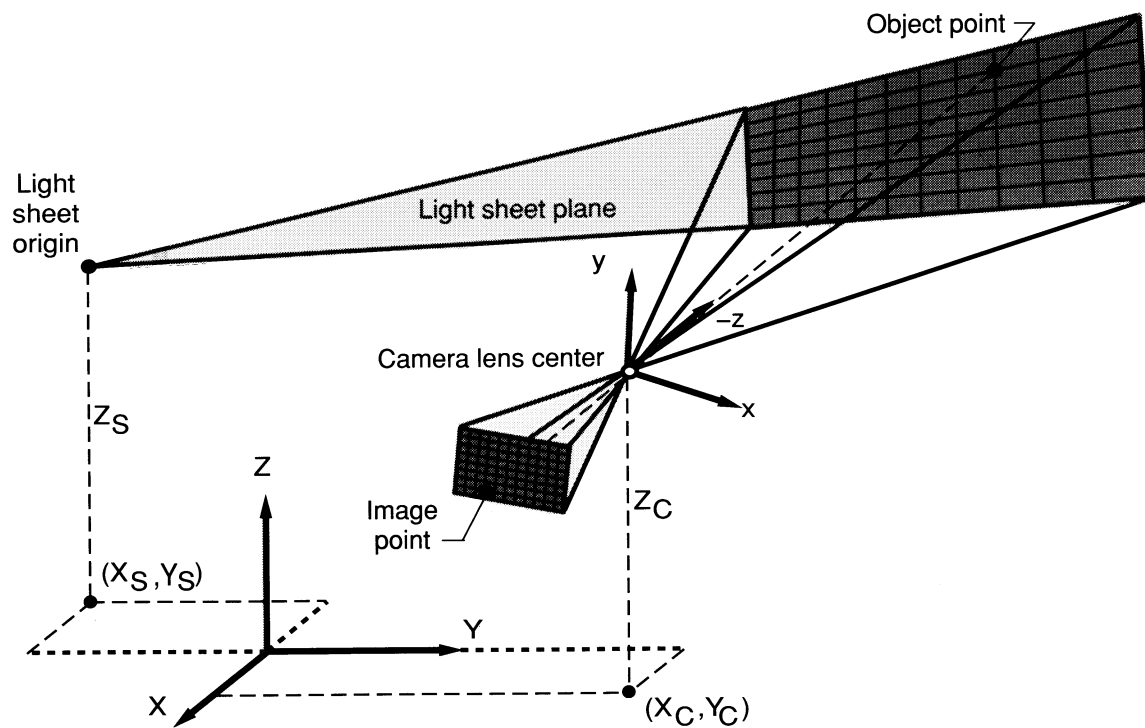


Figure 1. Typical image and object space geometry.

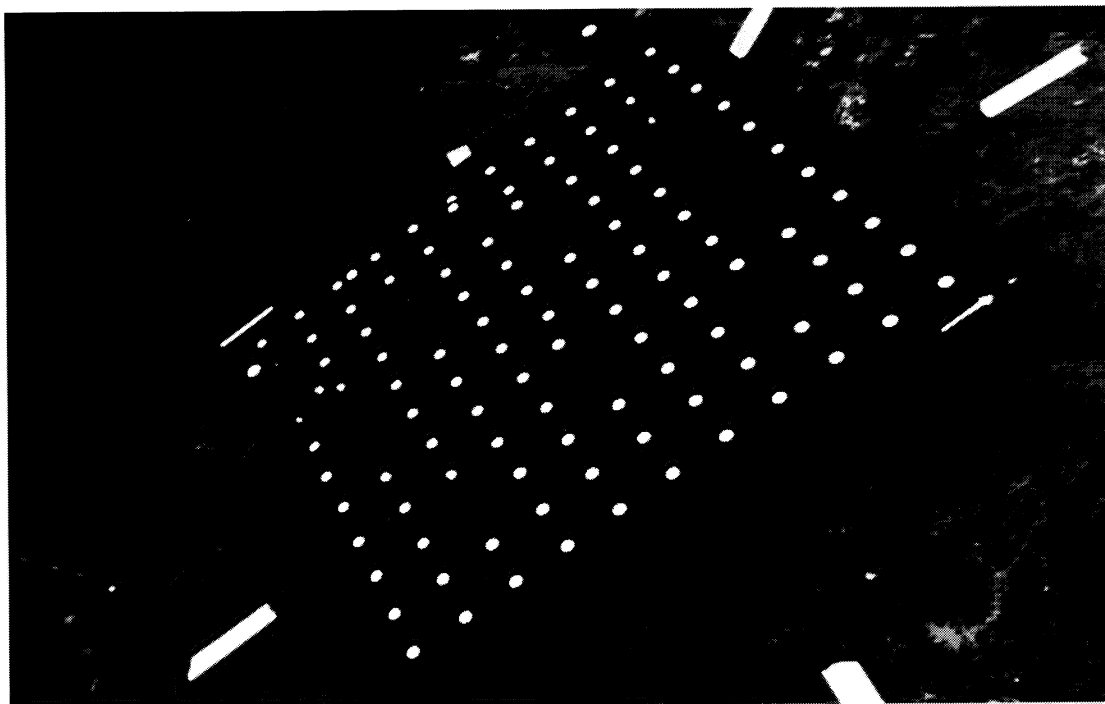
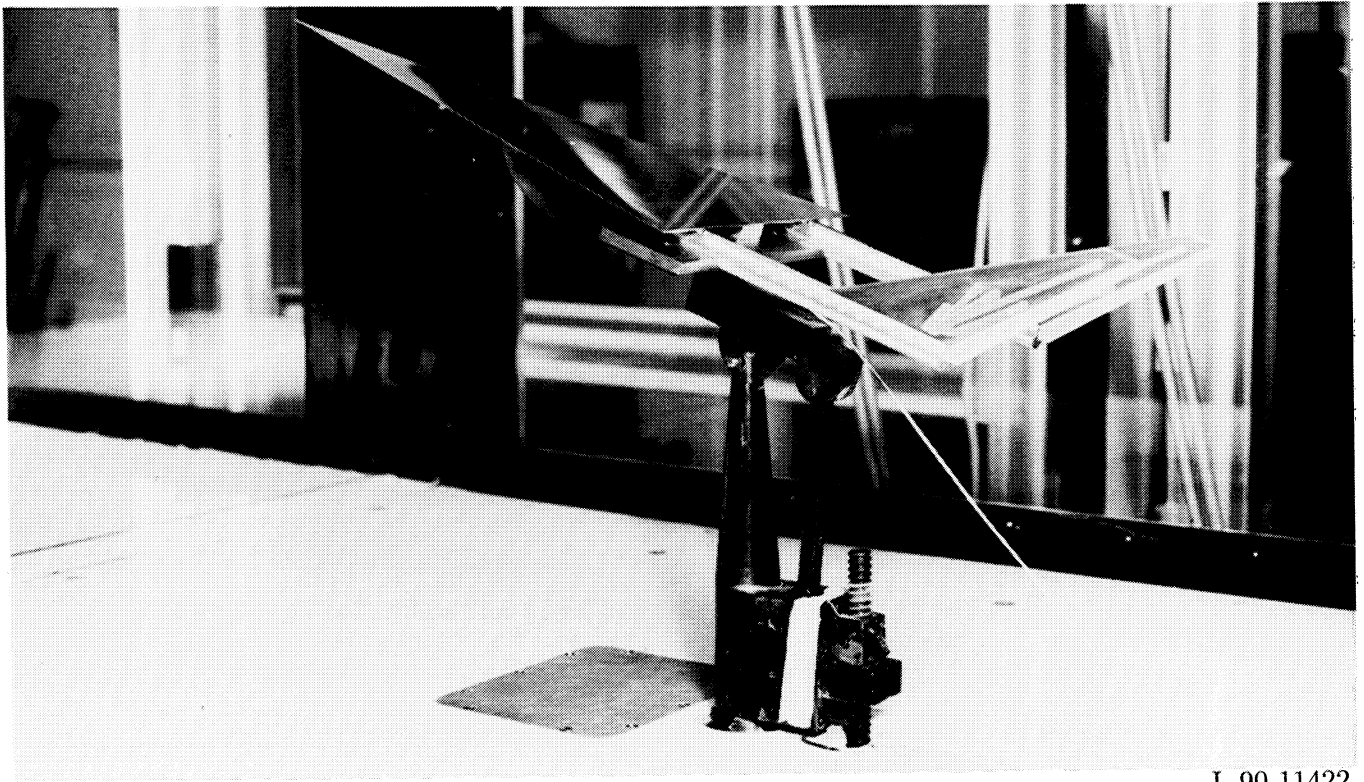


Figure 2. Image of typical calibration target plate from one station.



L-90-11422

Figure 3. The 76° flat delta wing with twin vertical tails mounted in BART test section.

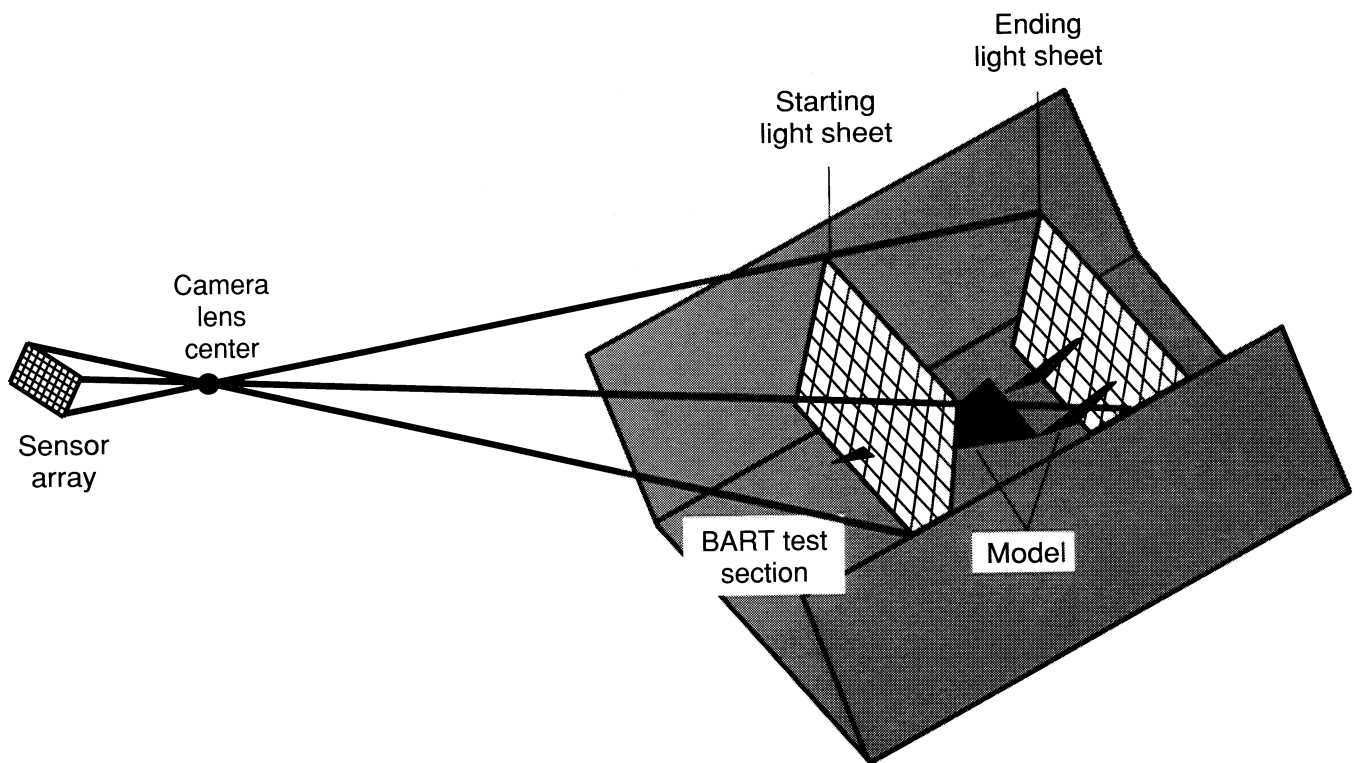
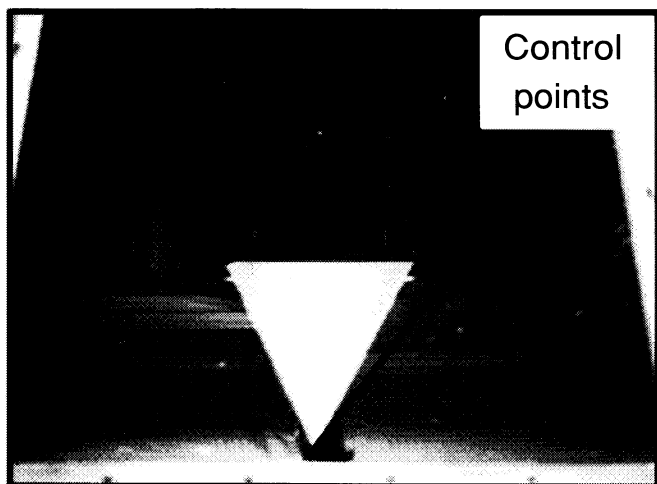
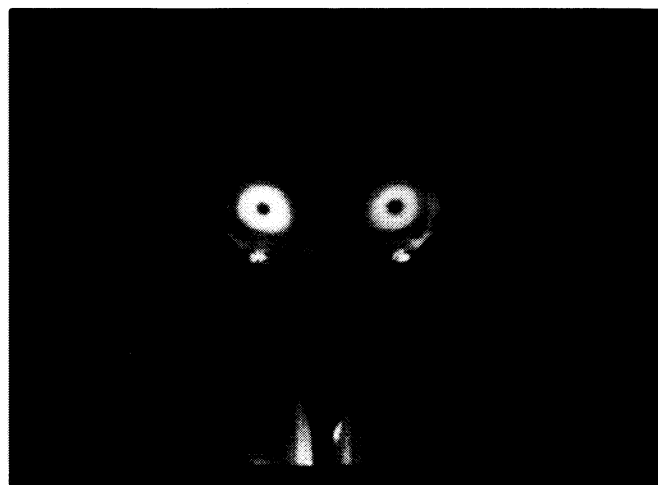


Figure 4. BART experimental geometry for  $\alpha = 20^\circ$ .



(a) Delta wing model in test section with lights on.



(b) Light sheet image for station  $S = 1.1$ .

Figure 5. Visual image data recorded during BART experiment.

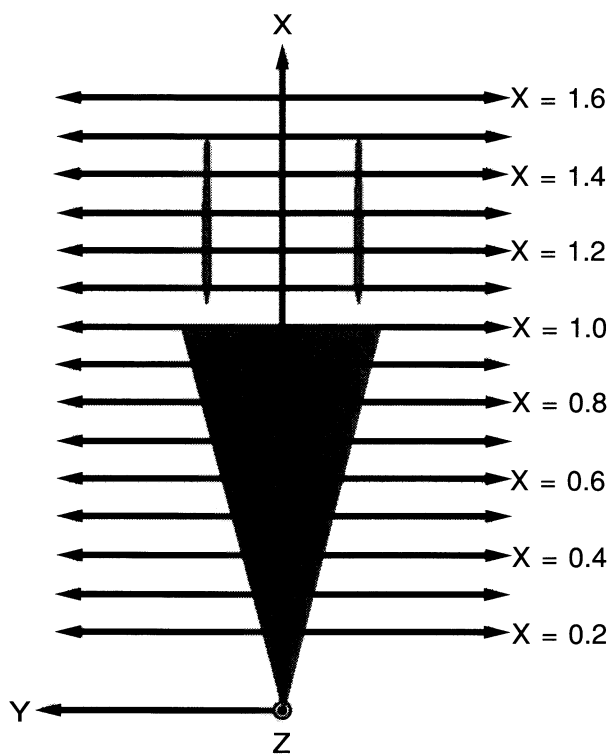
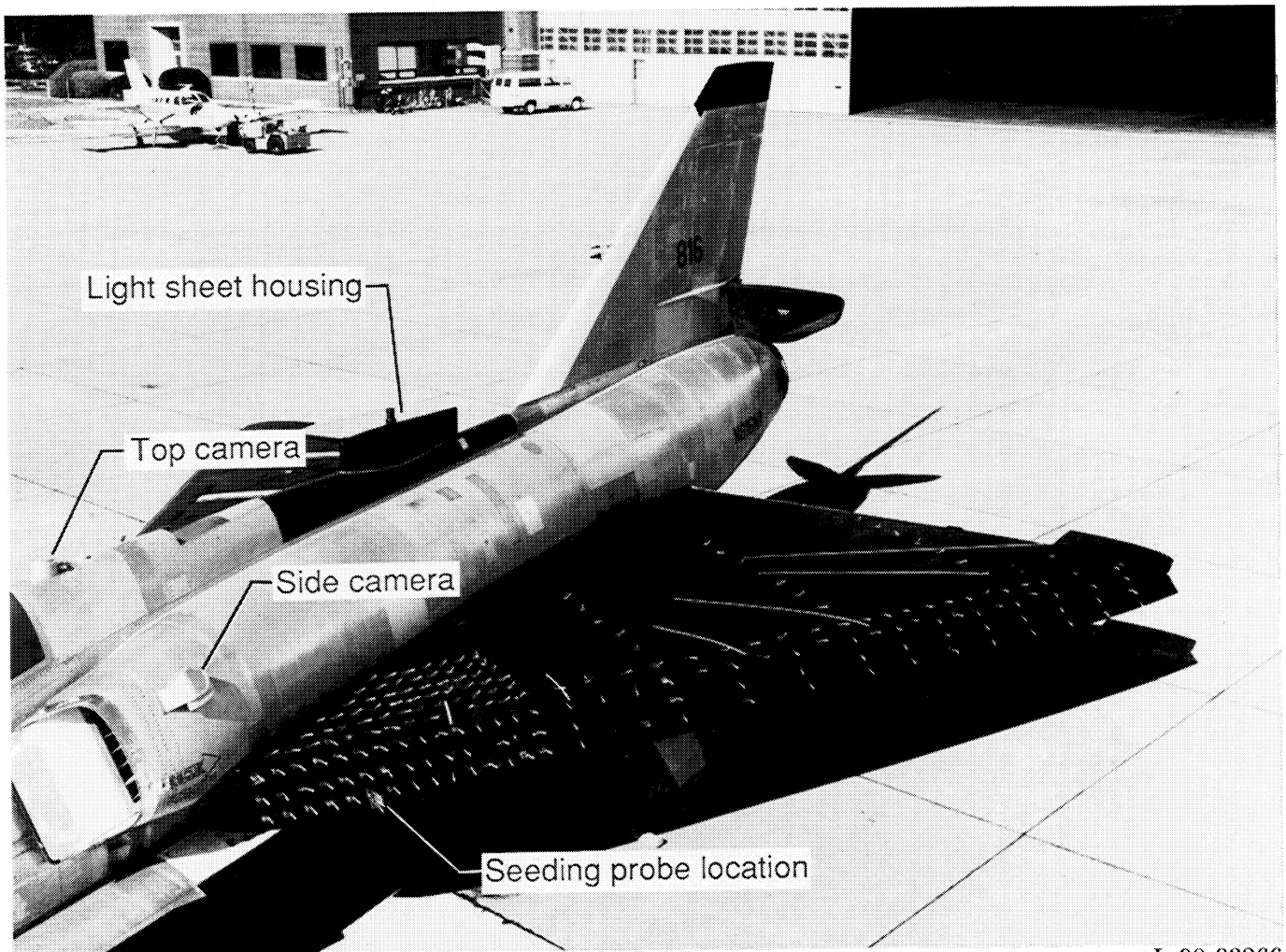


Figure 6. Schematic of  $76^\circ$  delta wing model coordinate system.





L-90-03266

Figure 7. Photograph of F-106B aircraft.

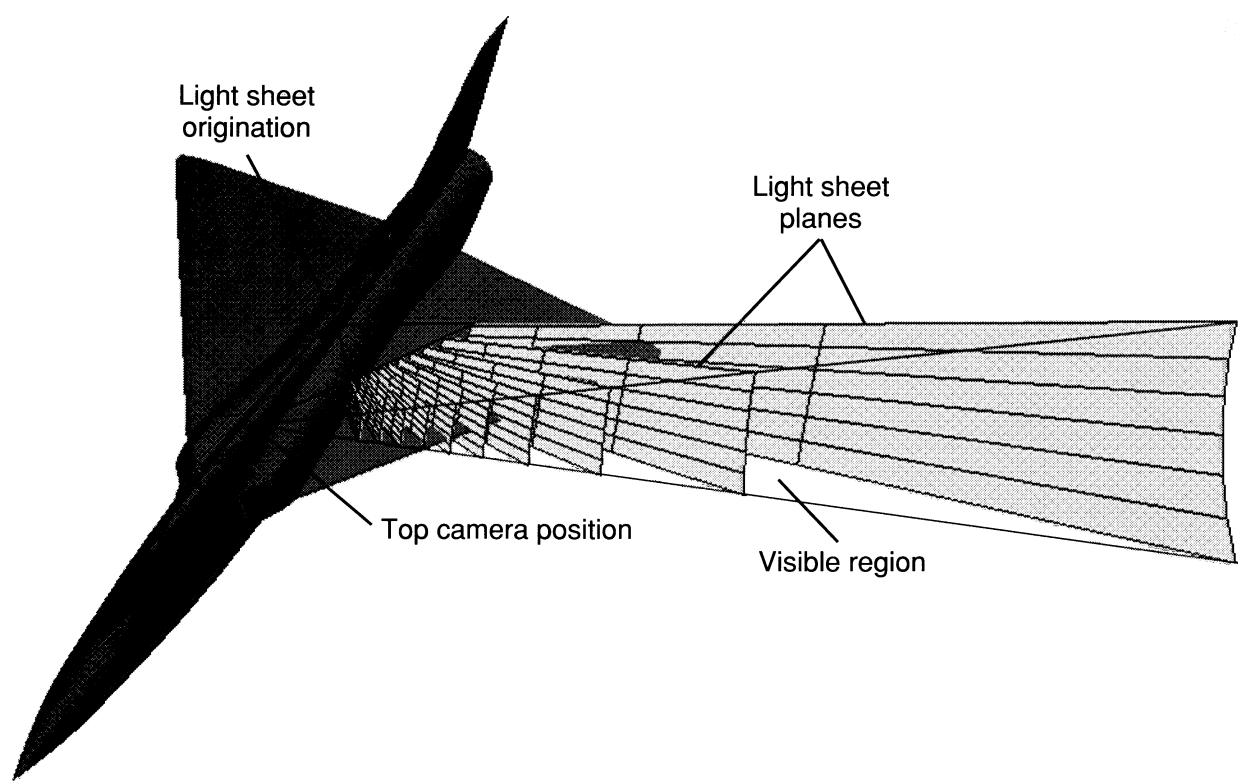
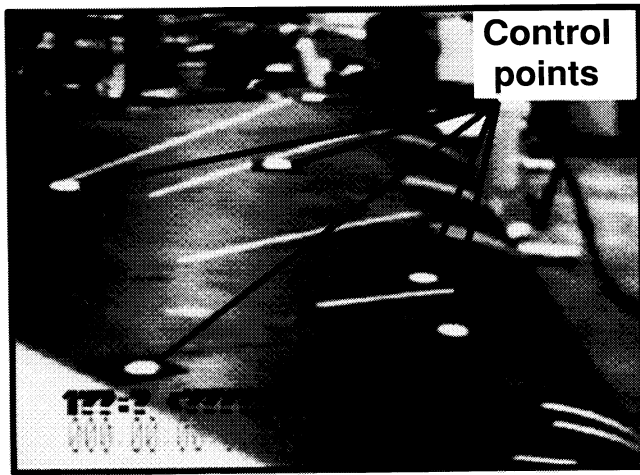
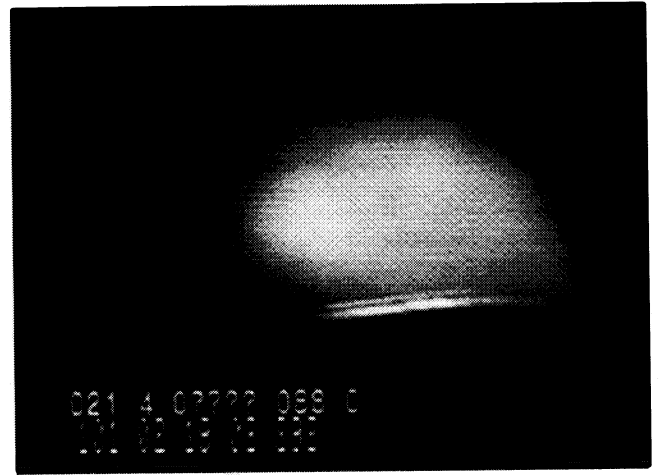


Figure 8. The F-106B aircraft experimental geometry for top camera.



(a) The port wing of F-106B aircraft taken on ground.



(b) Light sheet image for  $\Phi = 91^\circ$ .

Figure 9. Visual image data for F-106B aircraft in-flight experiment.

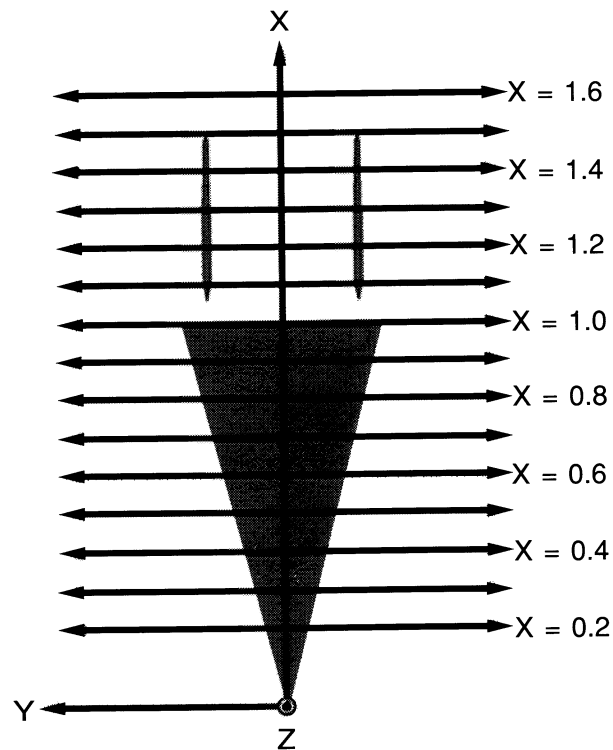


Figure 10. Schematic of F-106B aircraft coordinate system and light sheet stations.

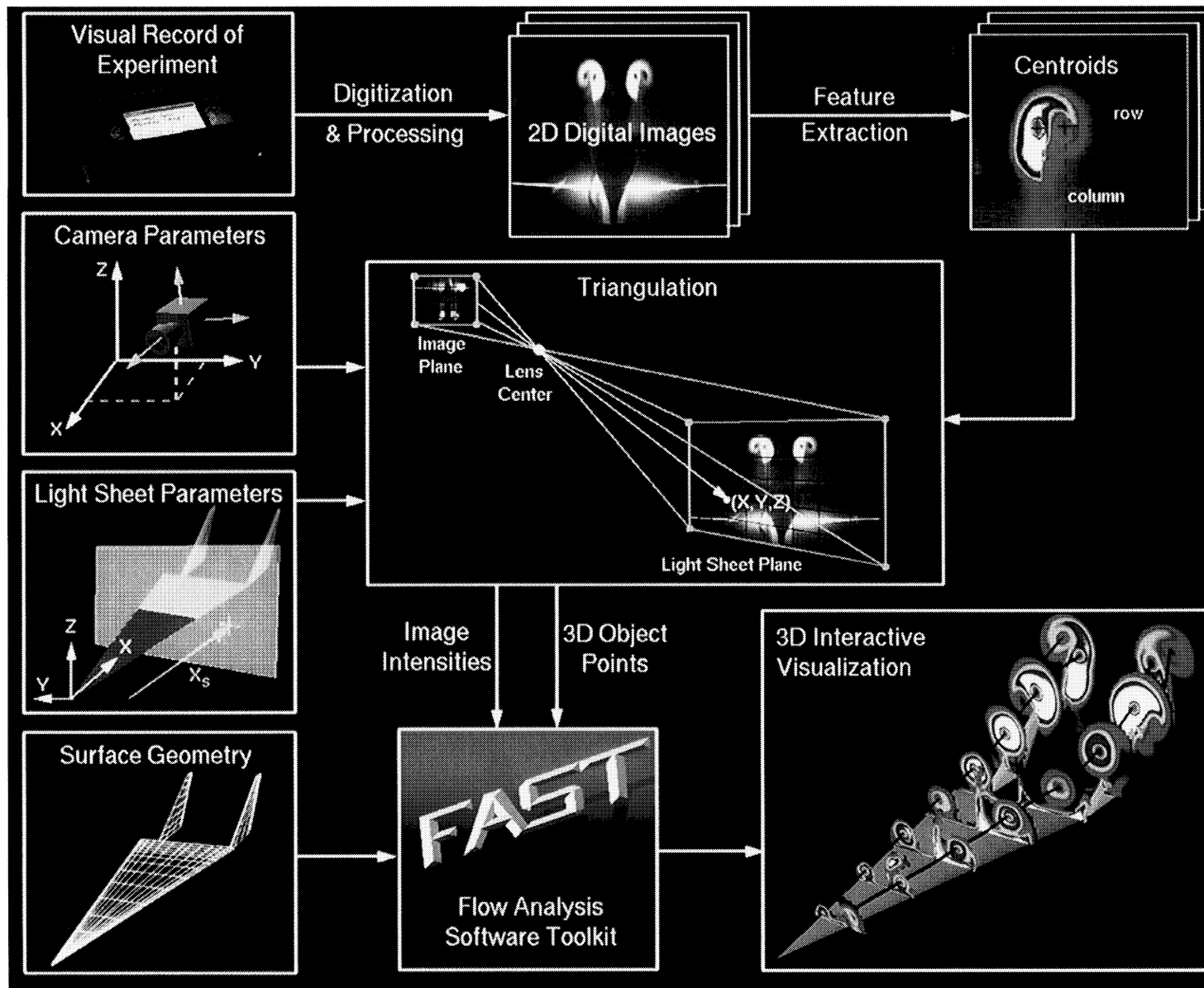


Figure 11. Diagram of computer visualization process.

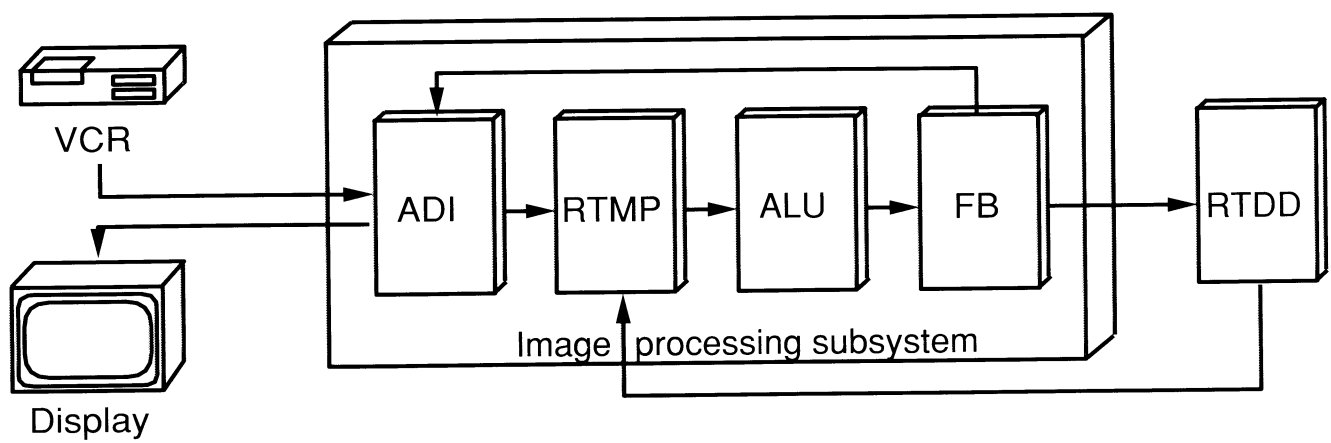


Figure 12. Configuration of image processing pipeline.

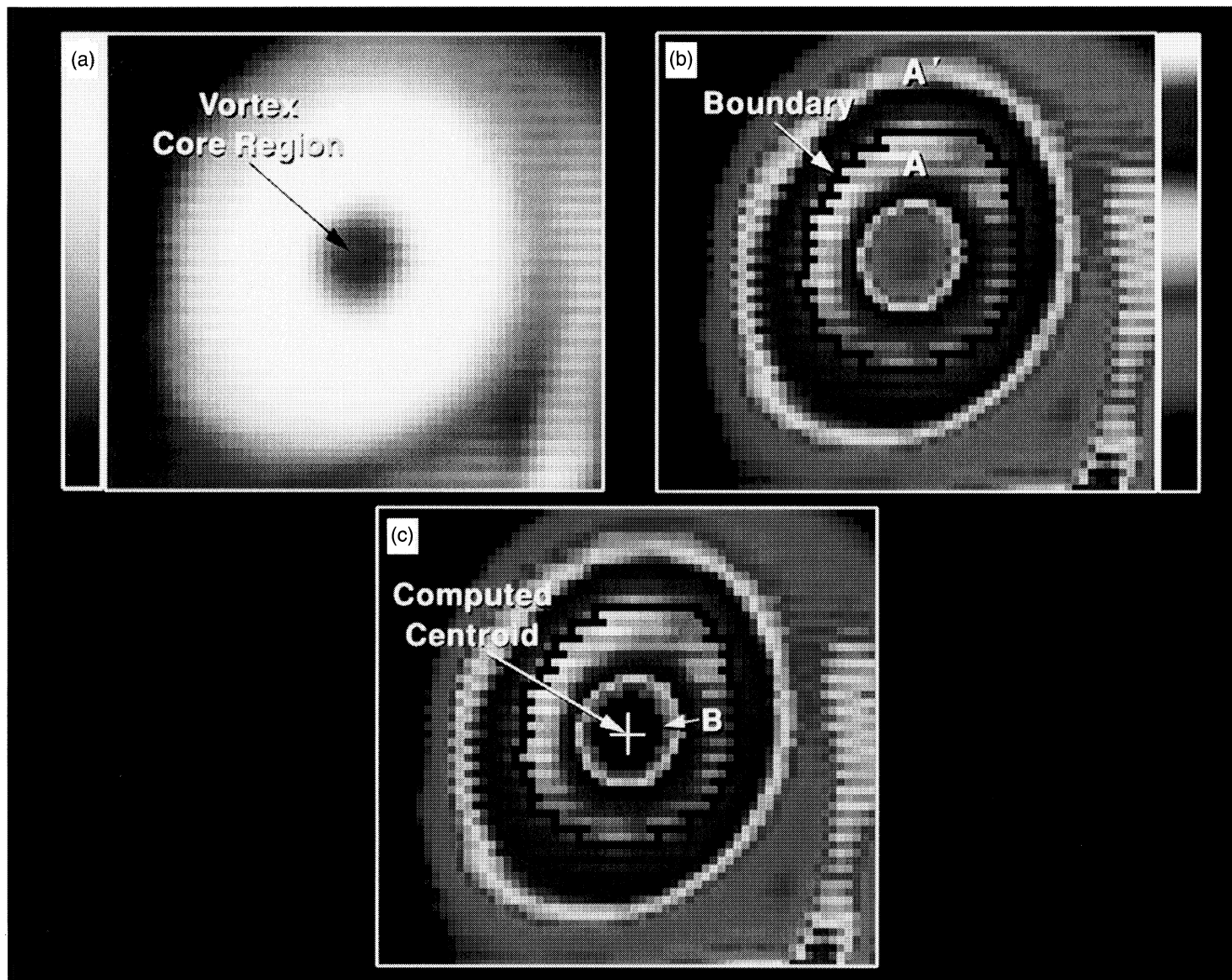


Figure 13. Steps for determining subset of pixels used in computing centroid; (a) enlarged gray-scale image of port side vortex core region; (b) subset A; (c) subset B (crosshair marks computed location of vortex core).

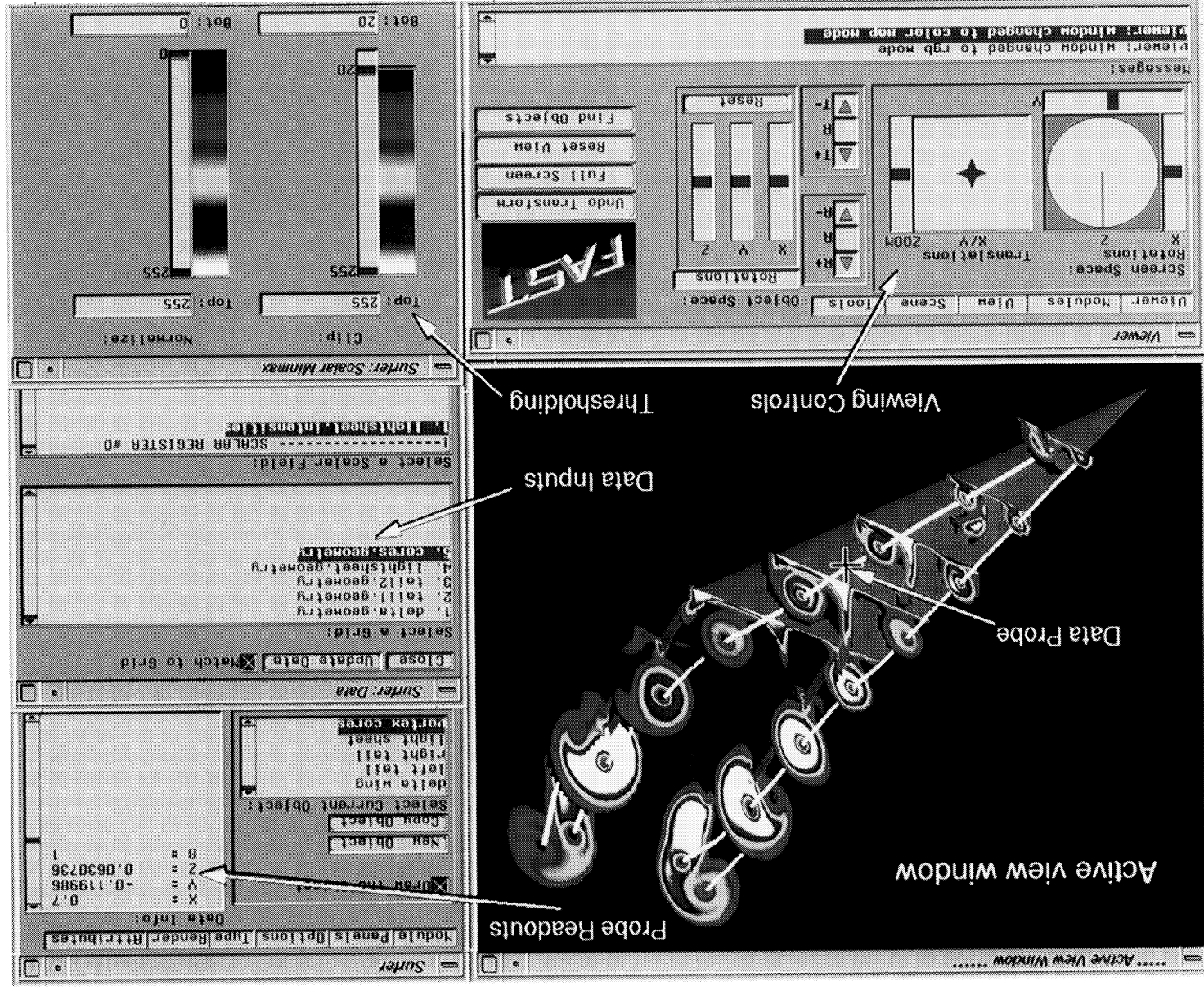


Figure 14. FAST postprocessing graphics environment used to analyze experimental data sets.

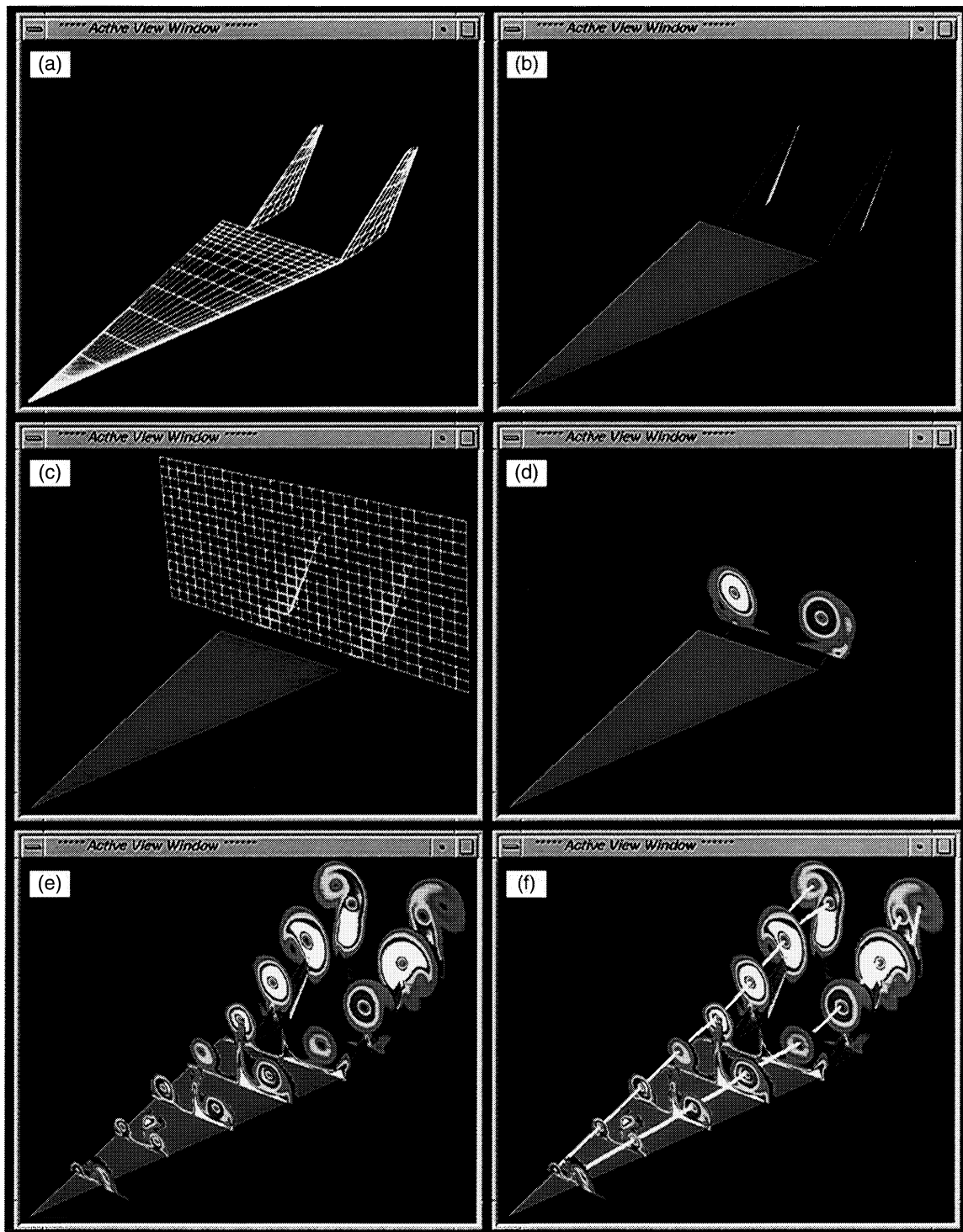


Figure 15. FAST *Active View Windows* for BART experimental data sets; (a) model grid lines; (b) smooth shaded model; (c) light sheet grid for station  $X = 1.1$ ; (d) interpolated function values; (e) clipped function values for every other light sheet station; (f) vortex core paths.



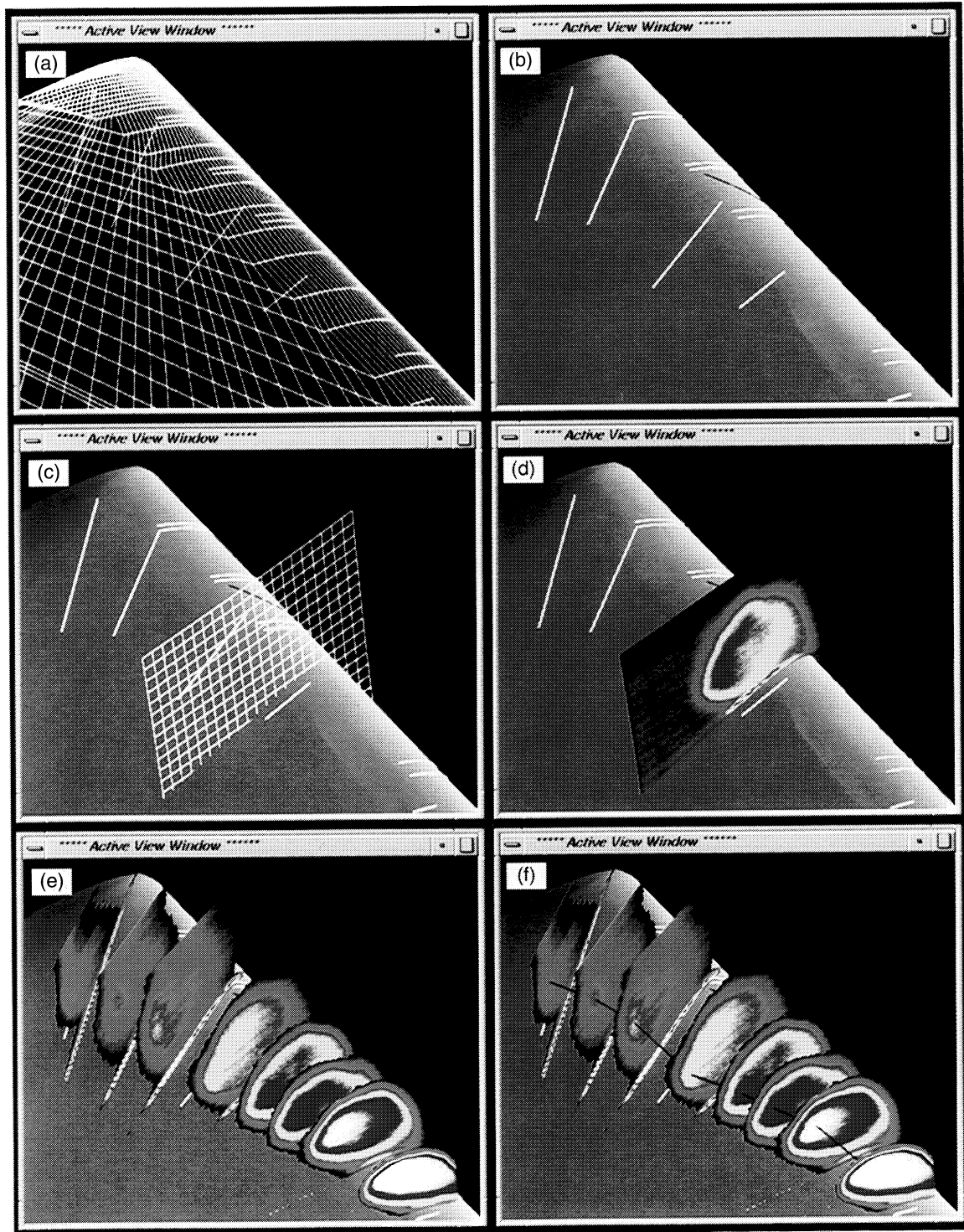


Figure 16. FAST *Active View Windows* for F-106B aircraft experimental data sets; (a) port wing grid lines; (b) smooth shaded wing; (c) light sheet grid for  $\Phi = 91^\circ$ ; (d) interpolated function values; (e) clipped function values for multiple light sheet locations; (f) vortex core paths.

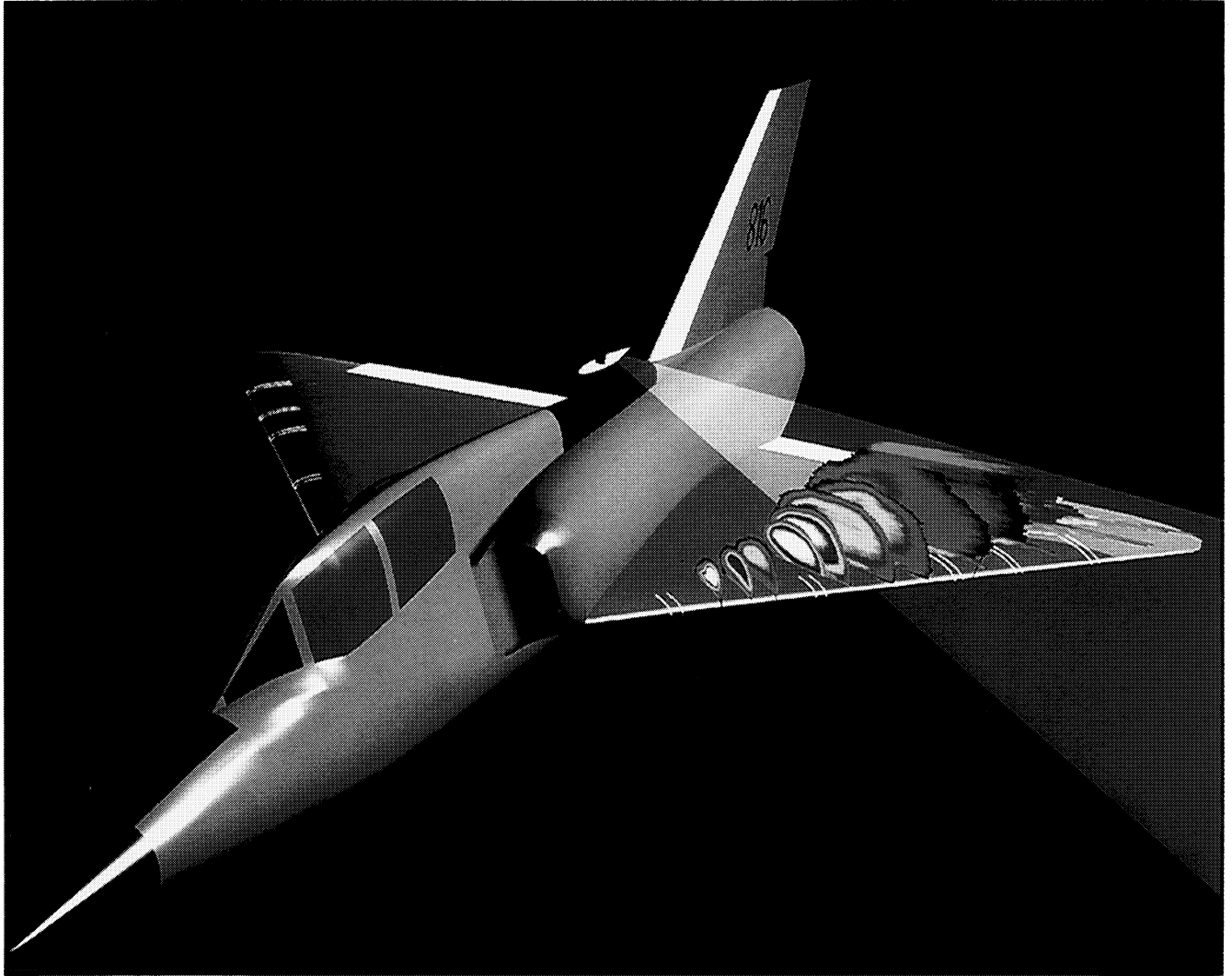
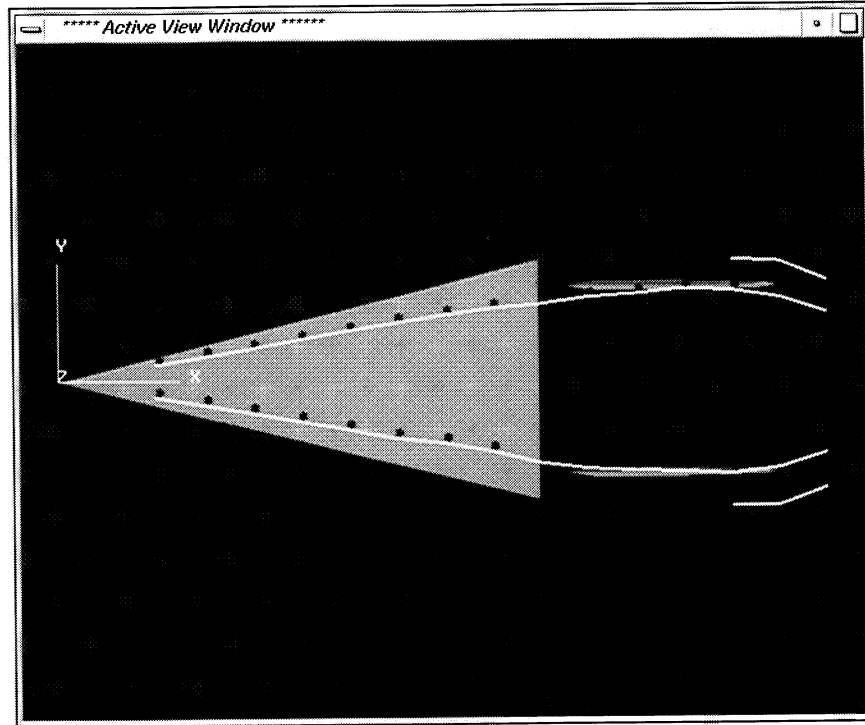
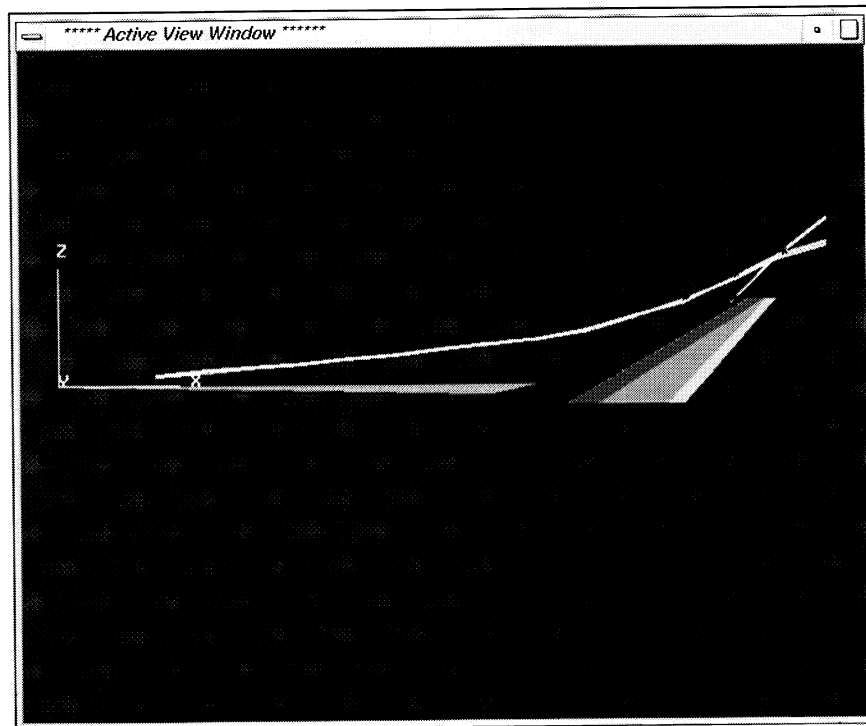


Figure 17. View of F-106B aircraft with vapor-screen images superimposed.



(a) Top view.



(b) Side view.

Figure 18. BART delta wing with reconstructed vortex core paths.

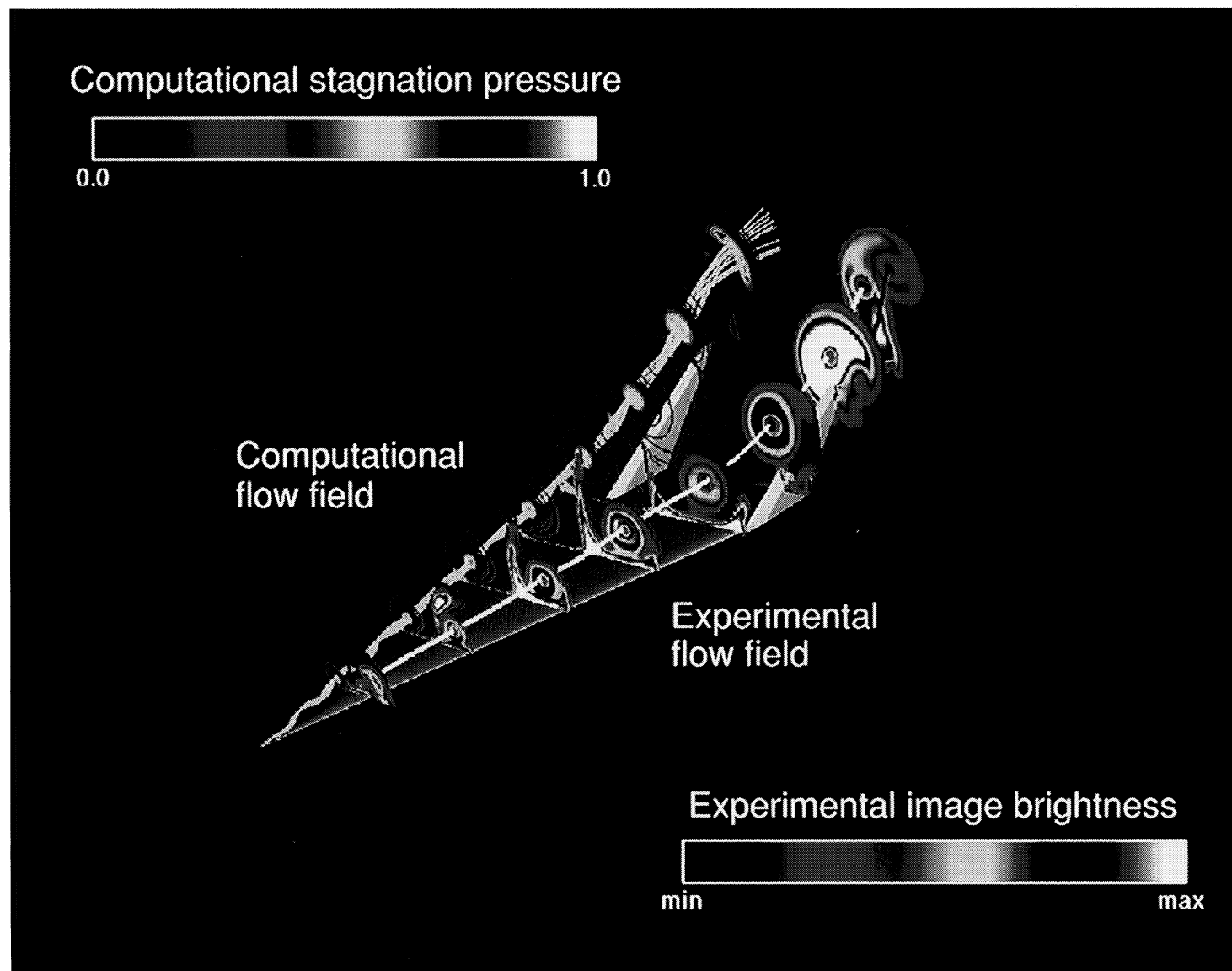
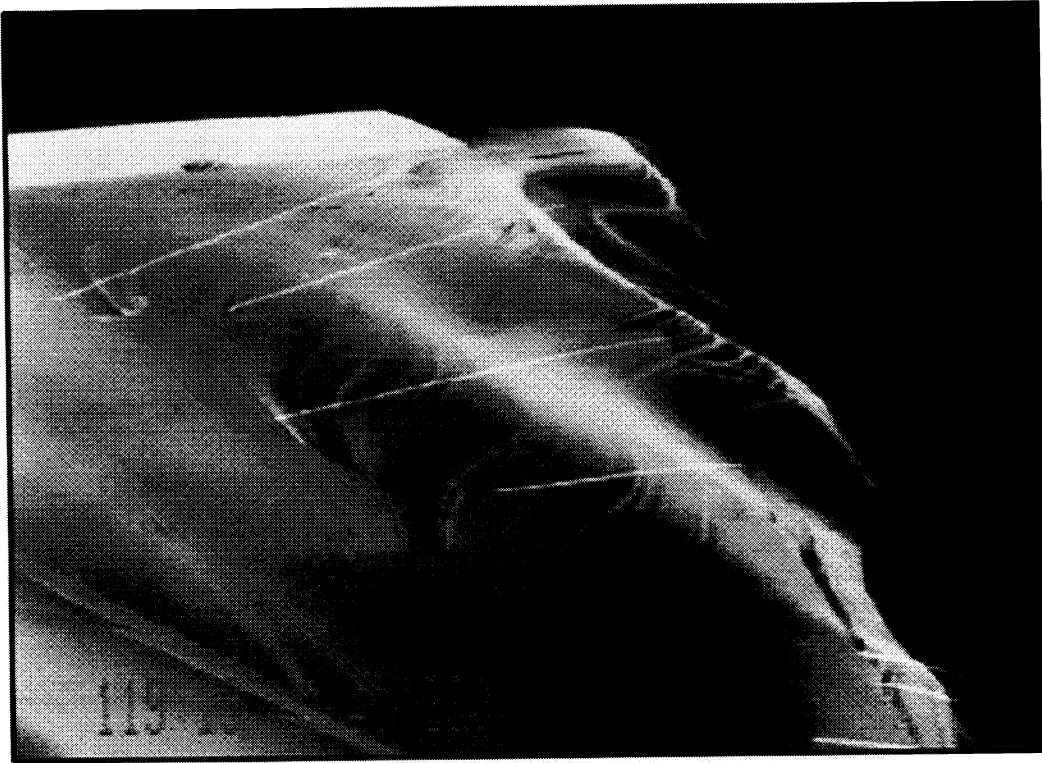
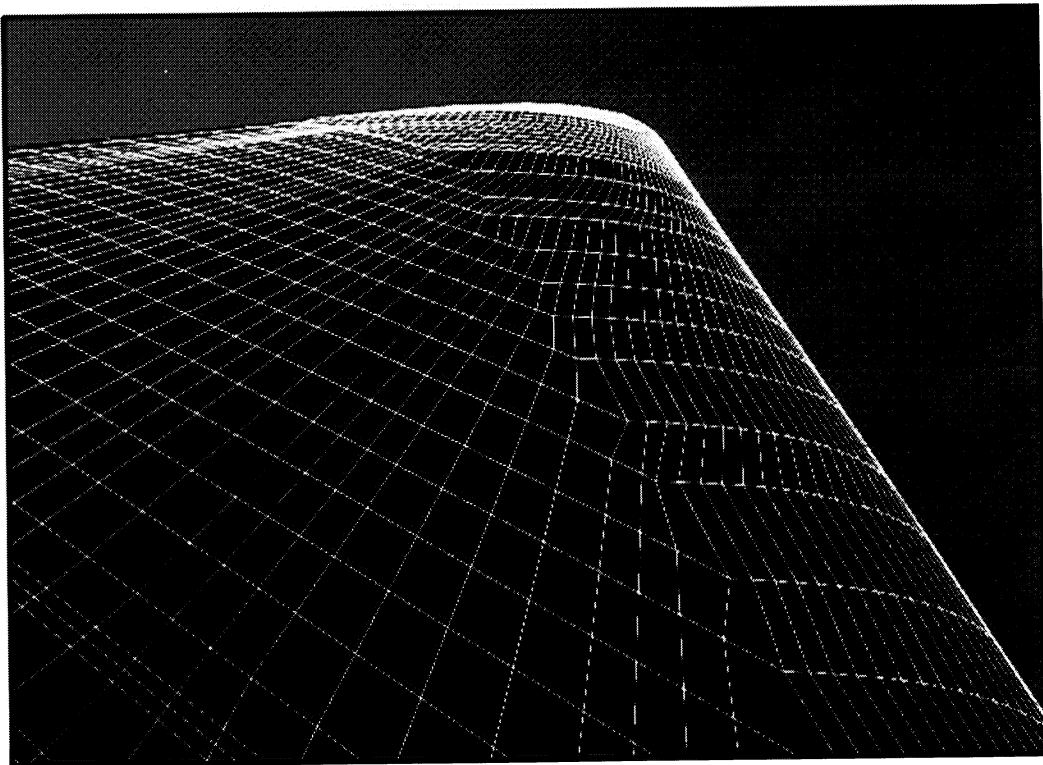


Figure 19. Reconstructed experimental light sheet images from FAST with computational stagnation pressure contours on 76° delta wing model.

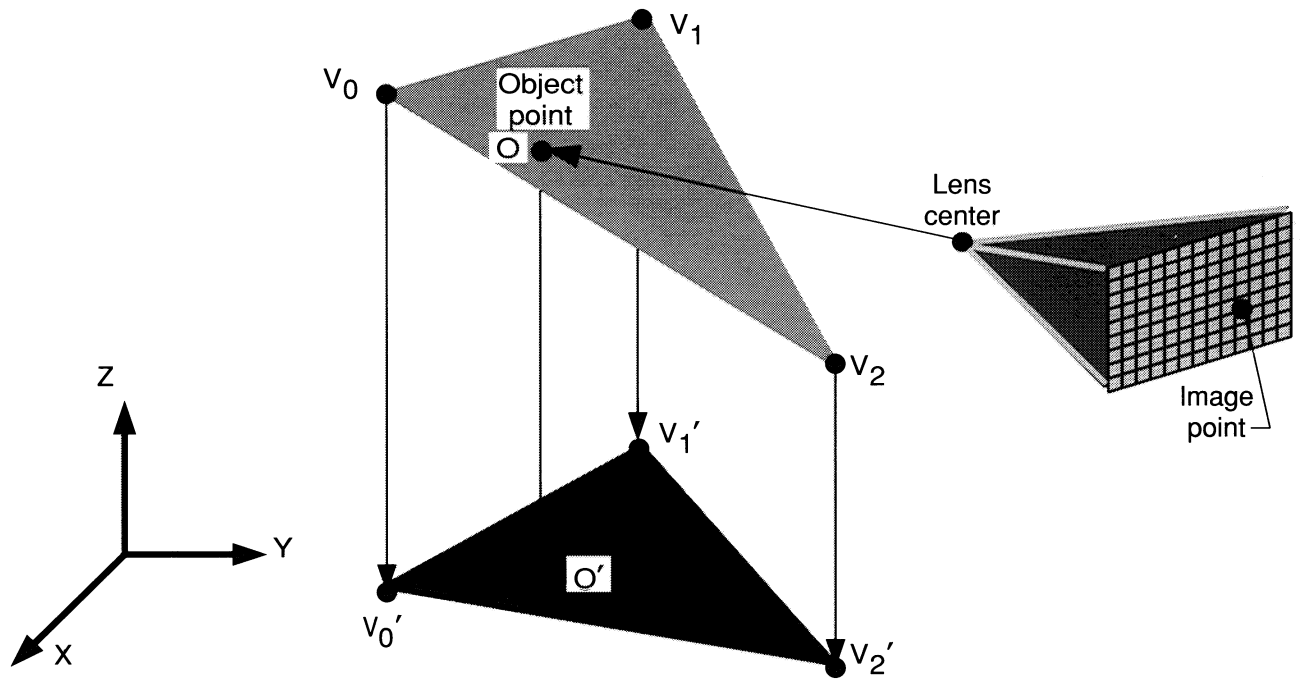


(a) Oil-flow image acquired from top camera.

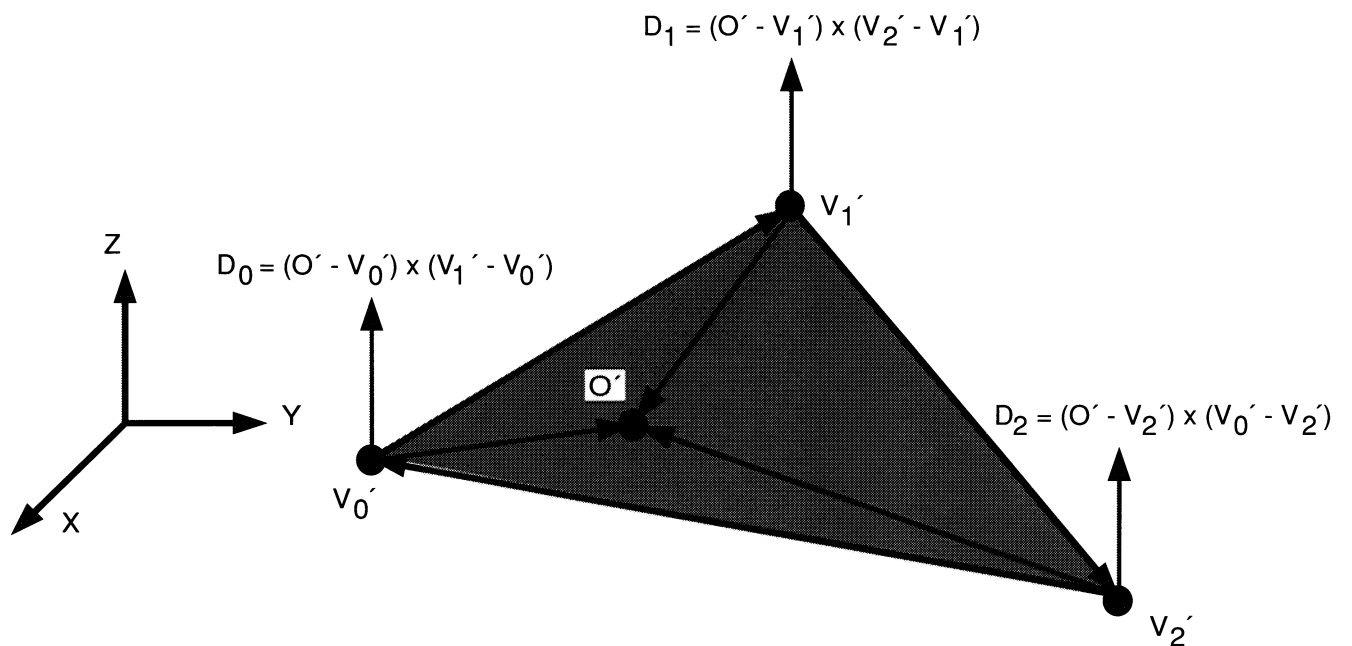


(b) Numerical surface geometry that approximates port wing.

Figure 20. Actual and simulated views of F-106B aircraft port wing.

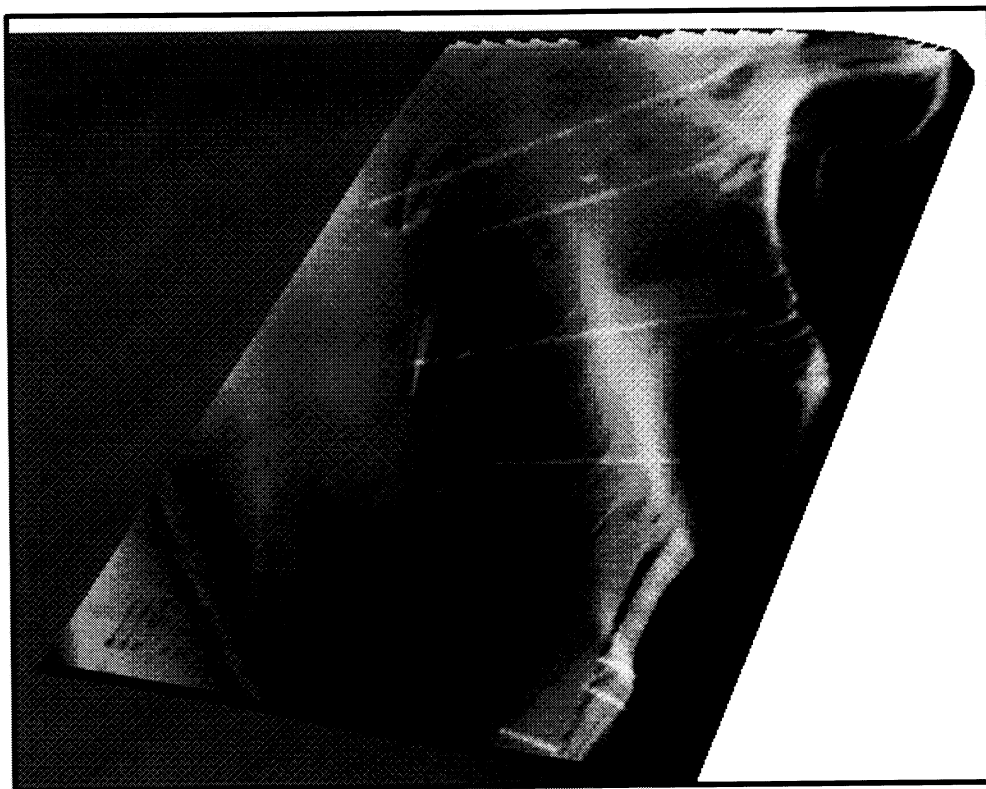


(a) Orthographic projection of object point and triangle vertices.

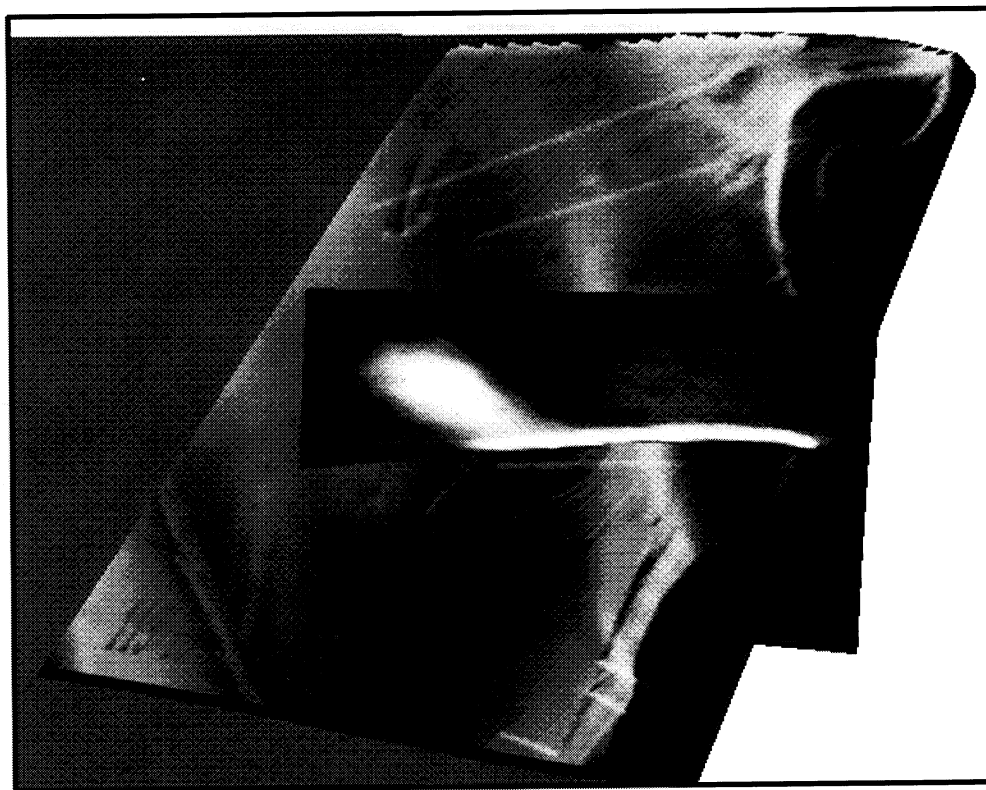


(b) Calculation of cross products for each triangle vertex.

Figure 21. Steps in determining proximity of object point with respect to triangle.



(a) Oil-flow mapped onto port wing.



(b) Superposition of reconstructed oil-flow image and vapor-screen image.

Figure 22. View from FAST of reconstructed images for F-106B aircraft.

REPORT DOCUMENTATION PAGE			Form Approved OMB No. 0704-0188	
Public reporting burden for this collection of information is estimated to average 1 hour per response, including the time for reviewing instructions, searching existing data sources, gathering and maintaining the data needed, and completing and reviewing the collection of information. Send comments regarding this burden estimate or any other aspect of this collection of information, including suggestions for reducing this burden, to Washington Headquarters Services, Directorate for Information Operations and Reports, 1215 Jefferson Davis Highway, Suite 1204, Arlington, VA 22202-4302, and to the Office of Management and Budget, Paperwork Reduction Project (0704-0188), Washington, DC 20503.				
1. AGENCY USE ONLY(Leave blank)	2. REPORT DATE July 1994	3. REPORT TYPE AND DATES COVERED Technical Paper		
4. TITLE AND SUBTITLE Computer-Aided Light Sheet Flow Visualization Using Photogrammetry		5. FUNDING NUMBERS  WU 505-90-53-02		
6. AUTHOR(S) Kathryn Stacy, Kurt Severance, and Brooks A. Childers				
7. PERFORMING ORGANIZATION NAME(S) AND ADDRESS(ES) NASA Langley Research Center Hampton, VA 23681-0001		8. PERFORMING ORGANIZATION REPORT NUMBER  L-17291		
9. SPONSORING/MONITORING AGENCY NAME(S) AND ADDRESS(ES) National Aeronautics and Space Administration Washington, DC 20546-0001		10. SPONSORING/MONITORING AGENCY REPORT NUMBER NASA TP-3416		
11. SUPPLEMENTARY NOTES				
12a. DISTRIBUTION/AVAILABILITY STATEMENT  Unclassified-Unlimited  Subject Category 61			12b. DISTRIBUTION CODE	
13. ABSTRACT (Maximum 200 words) A computer-aided flow visualization process has been developed to analyze video images acquired from rotating and translating light sheet visualization systems. The computer process integrates a mathematical model for image reconstruction, advanced computer graphics concepts, and digital image processing to provide a quantitative and a visual analysis capability. The image reconstruction model, based on photogrammetry, uses knowledge of the camera and light sheet locations and orientations to project two-dimensional light sheet video images into three-dimensional space. A sophisticated computer visualization package, commonly used to analyze computational fluid dynamics (CFD) results, was chosen to interactively display the reconstructed light sheet images with the numerical surface geometry for the model or aircraft under study. The photogrammetric reconstruction technique and the image processing and computer graphics techniques and equipment are described. Results of the computer-aided process applied to both a wind tunnel translating light sheet experiment and an in-flight rotating light sheet experiment are presented. The capability to compare reconstructed experimental light sheet images with CFD solutions in the same graphics environment is also demonstrated.				
14. SUBJECT TERMS Light sheet flow visualization; Three-dimensional reconstruction; Digital image processing; Photogrammetry			15. NUMBER OF PAGES 34	
			16. PRICE CODE A03	
17. SECURITY CLASSIFICATION OF REPORT Unclassified	18. SECURITY CLASSIFICATION OF THIS PAGE Unclassified	19. SECURITY CLASSIFICATION OF ABSTRACT	20. LIMITATION OF ABSTRACT	